; revised .

Millimeter-wave V2X Channel Measurements in Urban Environments

(invited paper)

Andreas F. Molisch,* ***Fellow, IEEE*****, Christoph F. Mecklenbräuker,**† ***Senior Member, IEEE*****, Thomas Zemen,**‡ ***Senior Member, IEEE*****, Aleš Prokes,**§ **Markus Hofer,**‡ **Faruk Pasic,** ***Graduate Student Member, IEEE*****,**† **and Hussein Hammoud,***

[1]Ming Hsieh Dept. of Electrical and Computer Engineering, University of Southern California, Los Angeles, CA, USA, email: {molisch, hhammoud }@usc.edu.
[2]Institute of Telecommunications, TU Wien, Vienna, Austria, email: {cfm, faruk.pasic}@tuwien.ac.at.
[3]AIT Austrian Institute of Technology GmbH, Austria, email: {Thomas.Zemen,Markus.Hofer}@ait.ac.at.
[4]Dept. of Radio Electronics, Brno University of Technology, Czech Republic, email: prokes@vut.cz.

CORRESPONDING AUTHOR: Andreas F. Molisch (e-mail: molisch@usc.edu).

The work of A. F. Molisch and H. Hammoud was supported by the California Transportation Authority through the METRANS program, and by the National Science Foundation through projects 1926913 and 2106602. The work of M. Hofer and T. Zemen is supported by the DEDICATE project funded within the Principal Scientist Grant "Dependable wireless 6G communication systems" at the AIT Austrian Institute of Technology. The work of A. Prokes was supported by the Czech Science Foundation for supporting our research through project 23-04304L.

ABSTRACT Vehicle-to-everything (V2X) communications is an important part of future driver assistance and traffic control systems that will reduce accidents and congestion. The millimeter-wave (mmWave) band shows great promise to enable the high-data-rate links that are required or at least beneficial for such systems. To design such systems, we first need a detailed understanding of the vehicle-to-vehicle (V2V) and vehicle-to-infrastructure (V2X) propatation channels. This paper provides a systematic account of a series of measurement campaigns for such channels, conducted by the four research institutions of the authors over the past year. After a description of the similarities and differences of the channel sounders used in the campaigns, a description of the measurements in two European and one American city is given, and the scenarios of convoy, opposite-lane passing, and overtaking, are described. This is then followed by key results, presenting both sample results of power delay profiles and delay Doppler (or angular) spectra, as well as the statistical description such as delay spread and size of stationarity region. We also discuss the availability of spatial diversity in V2I connections and the correlation of the channels between different frequency bands.

INDEX TERMS channel measurements, double-directional, channel modelling, mmWave, dynamic channels, V2V

I. Introduction

A. Motivation

Much has changed over the past years about vehicles and vehicle traffic - not only driver-assistance systems and autonomous driving, but also the shift from combustion engine to hybrid and electric vehicles, and from people driving to shops to delivery vehicles bringing the goods to the customers. However, the fundamental challenges, namely traffic congestion and accidents, have remained, as has the need to combat them. One of the most promising tools for tackling this goal is vehicle-to-vehicle (V2V) and vehicle-to-infrastructure (V2I) communications, together known as vehicle-to-everything (V2X). Constant communication of vehicles with each other is especially important for accident avoidance through coordination of lane changes, warning of obstacles, etc., while communication with infrastructure that knows large-scale traffic situations and can re-direct traffic can alleviate traffic congestion, saving time and reducing pollution.

While previous attempts at V2X communication, such as the wireless access in vehicular environments (WAVE) system [1], mainly focused on short messages, recent years have shown the need for transmitting large amounts of data, including streams of camera pictures, radar and lidar images, etc., over the air. This, combined with the large number of vehicles wishing to communicate in a small area, leads to a huge amount of total traffic that requires in turn large amounts of spectrum. The millimeter wave (mmWave) band is the band that (i) has such resources available, and (ii) is already used for both cellular 5G new radio (NR) and wireless local area network (WLAN) 802.11 systems; it is thus expected to form the (or at least a) backbone of future V2X communications.

It is axiomatic that the development of wireless systems requires an understanding of, and model for, the radio propagation channel in which the system operates. Aspects ranging from antenna and array design, to waveform parameter definitions (e.g., subcarrier spacing to avoid significant intercarrier interference) to signal processing algorithms such as precoding, all depend on the particular properties of the propagation channels. Yet V2X mmWave channels are relatively little explored. While some important work has been done (see the literature survey in Sec. II), the available measurements on which all models must rest do not cover all scenarios of interest, much less provide enough data for statistical reliability or training of machine learning models. Thus, there is a significant need for more measurements.

To alleviate this gap, the wireless groups of four research institutions - Technical University Vienna (TUW), Austrian Institute of Technology (AIT), Brno University of Technology (BUT), and University of Southern California (USC) collaborated over the past five years on a series of measurement campaigns. The collaboration included exchange of ideas for channel sounder construction, joint planning of measurement campaigns (to have some comparable measurements in different cities, and otherwise avoid excessive overlap between the measured scenarios), as well as joint evaluation and interpretation of the measurements. Results from these campaigns were presented in a series of research papers [2]–[14]. The aim of the current paper is to systematically present and compare the channel sounders, measurement scenarios, and results of those campaigns.

B. Contributions

Thus, the main contributions of this paper are as follows:

- We present the generic channel sounder structure we used, as well as pros and cons of the individual design choices of the four different sounders that were realized as part of this project. This includes a novel sounder structure called Redirecting Rotating Mirror Arrangement (ReRoMA) that is particularly suited for low-cost directionally resolved measurements at high frequencies.
- We present time-variant channel impulse response (CIR) and their physical interpretations for a variety of measurement scenarios. We demonstrate that in many cases the main reflecting/scattering objects can be well identified, and show that objects that might not be very significant at lower frequencies can be highly relevant or even dominant at mmWave frequencies.
- We evaluate and compare the statistics of the measured channels, including pathloss, and root mean square (RMS) delay spread and Doppler spread, as well as stationarity regions.
- For V2I channels, we analyze the impact of antenna diversity at the infrastructure node, as well as the correlations between different centimeter wave (cmWave) and mmWave bands.

C. Organization of the paper

The remainder of the paper is organized as follows: Sec. II provides an overview of the existing literature for mmWave V2X channel measurements. Section III summarizes the four sounders developed by the consortium members, while Sec. IV describes the environments and vehicle trajectories of the measurements. Section V summarizes the evaluation procedures and definitions of the key channel quantities. Finally, Section VI provides representative examples of the measurement results; conclusions are drawn in Sec. VII.

II. State of the Art

V2V propagation channels below 6 GHz have been extensively researched, with both modeling methodology and measurement results summarized in several surveys [1], [15]–[19]. Studies in this frequency range are relevant for mmWave investigations both because they discuss typical operating scenarios, and for purpose of comparison of the (statistical) results. It must be noted that V2V scenarios have been measured much more than V2I, possibly because V2I is considered to be similar to the traditional urban microcellular setup. There are far fewer surveys for mmWave V2X channels; [20] provides an overview of the main challenges; the magazine paper [21] provides research results as well as several references; [19] includes some mmWave campaigns as part of an overview that contains all frequency ranges.

In contrast to measurements at lower frequencies, almost all mmWave V2X measurements are done with single-input single-output (SISO) sounders, i.e., one fixed antenna at transmitter (TX) and one at the receiver (RX). The use of omni-directional antennas in this context has the advantage that all multi-path components (MPCs) are captured. On the downside, the high isotropic pathloss at mmWave frequencies leads to lower signal-to-noise ratio (SNR) than at lower frequencies [22, Chapter 4]. This is not a major issue for narrowband measurements, but those can only provide pathloss, shadowing, and small-scale fading. For wideband measurements, which are required for measuring delay dispersion, this results in rather limited maximum

range between TX and RX. For this reason, a number of measurements have been done with horn antennas with fixed orientation at either one, or both, link ends. This approach (which we used also for several of the measurement campaigns presented in the current paper) has the advantage of increasing the SNR and thus allowing measurements over larger distances.

Measurements with horns at both link ends are in particular common if the position of the TX and RX relative to each other does not change significantly during the measurements (e.g., in a convoy measurement the lead car's antenna is pointing backward and the following car's antenna is pointing forward). Another popular configuration is a horn antenna at one link end and an omni antenna at the other. This is particularly relevant for V2I communications, where the horn is placed at the infrastructure node; the omnidirectional antenna at the vehicle can collect MPCs from all directions, and the Doppler spectrum provides information about the angular distribution of the MPCs. Note, however, that a setup with fixed directional antennas fails to capture MPCs arriving or departing at angles outside the horn antenna's beamwidth.

The most fundamental channel property is the pathloss, and this has been investigated for mmWave V2V channels for many years. Early work used a two-ray model [23], and later incorporated also height fluctuations of the street [24]–[26], and rough road surfaces [27], [28]; the model was also confirmed by (Wideband) measurements, that resolved two components [29]. Another approach is a standard pathloss fitting based on extensive measurements where the distance between the cars is continuously varied. [30] did such measurements on both highways and urban roads in Japan. Comparisons of pathloss at 2.4 and 39 GHz were given in [31], based on measurements with fixed horn antennas. Measurements of pathloss when cars are crossing, using omnidirectional antennas, were shown in [32].

Several papers have measured the wideband characteristics. Ref. [33] provides a few sample results of measured delay/Doppler characteristics obtained by dynamic measurements with omnidirectional antennas. Refs. [34] and [35] measure path loss, delay spread, as well as angular spread in a single street and a T-intersection, respectively. These measurements use a static measurement setup as they employ mechanically rotated horn antennas for achieving the directional resolution. A similar type of measurement, but in the THz band, was done in [36]. Ref. [37] performed multiband measurements of impulse responses with fixed horn antennas in a convoy configuration.

Dynamic measurements using horn antennas at both the transmitter and receiver in an open-field scenario were conducted in [38]. Dynamic measurements with a SIMO setup, i.e., a fixed horn antenna at the TX, and a 4x8 array at the RX, which are intended for integrated sensing and communication (ISAC) were recently presented in [39]. Furthermore, [40] presents a dynamic SIMO channel sounder based on software defined radio (SDR). A full dynamic multiple-input multiple-output (MIMO) sounder, capable of measuring a MIMO snapshot within 6 ms, was presented in [41]–[43], together with several sample results. The TX is mounted on the roof of a moving car, and the RX is positioned like a traffic sign. The measurement scenario is a street with vehicles parked on both sides of the road. For each scenario, the paper presents measurements of the channel transfer function (CTF) gain, the power delay profile (PDP), and the Doppler spread average function. Another dynamic MIMO sounder, utilizing a phased array structure, was introduced in [44].

The impact of blocking vehicles between TX and RX on pathloss and fading was investigated in [28], [45], [46], highlighting the importance of diffraction over and under the car; the measurements were narrowband, with fixed horn antennas at both link ends. More recently, [47] measured the impact of blockers on delay and angular spectrum, using either a multi-band ultra-wideband sounder with mechanically rotated horn antennas (in this case the setup was static), or a wideband (600 MHz, operating at 73 GHz) sounder with a 4-element array of horn antennas. Another measurement of blockage impact, using a static setup at 28 GHz, is described in [48]; it mostly considers blockage by the broadside of a vehicle. Extensive real-time measurements of the blockage of cross-street line-of-sight (LOS) links by various types of vehicles can be found in the very recent [49]; sample measurements in a similar scenario are in [50]. Blockage by road bridges was measured in [51], using fixed horn antennas.

The number of dedicated V2I measurements is very small, for the above-mentioned reasons. To our knowledge, only [52] performed such measurements, and those are narrowband and provide only a few sample results. Quite a few measurements of "microcellular" channels (which often include base station heights at latern mast height, i.e., similar to typical roadside units) provide valuable insights for V2I connections as well; we refer the interested reader to survey articles such as [53]–[55].

In addition to the measurements and measurement-based models, there are also many investigations based on ray tracing or further-simplified models. Those are beyond the scope of the current paper, and consequently not discussed here. The interested reader is pointed to the survey papers mentioned at the beginning of this section.

III. Sounders

Channel sounders may be constructed according to different principles, which each may have particular advantages in certain situations, or are chosen because some of their essential components are already available in the labs of the measurement team [56]. In the following we provide a brief overview of the common structure of the sounders used in our campaigns, which will then be followed by subsections

describing the special implementations in the sounders of the four consortium members.

The generic sounder, for which Figure 1 shows the different implementations, can be described as follows: at the TX side, a waveform generator (which can be an arbitrary waveform generator (AWG), signal generator, universal software radio peripheral (USRP), etc.) generates a sounding signal either as a (complex) baseband or as a real signal at a low intermediate frequency (IF); this sounding signal will be repeated periodically during the measurements. The signal is then upconverted, in one or more stages, to passband (radio frequency (RF)), by mixing with the output of a frequency synthesizer (potentially combined with a frequency multiplier). Filters in the different upconversion stages are used to reject signal copies at undesired (image) frequencies. The RF signal is then amplified by a power amplifier (PA) and transmitted from a suitable (horn or omni) antenna. At the RX, the process is reversed: the output from a suitable antenna is amplified with a low noise amplifier (LNA), downconverted to either an IF or baseband by mixing with a local oscillator signal (created similarly as at the TX), digitized (by a sampling scope, digitizer, or USRP), and stored for postprocessing. In all cases, precision frequency references (typically global positioning system (GPS)-disciplined rubidium (Rb) clocks) provide a 10 MHz reference signal that controls signal generator, digitizer, and frequency synthesizers.

The practical differences in the sounders lie in the particular components used, the chosen IFs, amplification factors and power levels, and detailed implementations how, e.g., in-phase and quadrature-phase (IQ) mixing is implemented. The more fundamental differences are in the choice of the sounding sequences and the used antennas. For the sounding sequence, time-domain sequences allow a direct determination of the CIR by correlating the received signal with the transmitted sequences; pseudo-noise (PN)-sequences are widely known, but in the BUT sounder we use complementary Golay sequences due to their zero non-periodic autocorrelation function. The other sounders use multi-tone sequences with flat spectrum and low peak-to-average power ratio (PAPR), similar to the Zadoff-Chu sequences used in long term evolution (LTE) and NR for channel estimation; they more immediately provide the CTF. The spacing of the subcarriers determines the maximum measurable excess delay (note that in this paper, delay is multiplied with the speed of light, so that it takes on dimension [meter] and eases its interpretation in the context of the measurement geometry). For the antennas, the sounders of BUT, TUW, and AIT do not provide angular resolution, but use an omnidirectional antenna at one link end (to collect MPCs from all directions), while the other link end typically uses a horn antenna to increase the SNR. Only the USC sounder setup provides directional resolution through a rotating setup as described in Sec. III.D.

A. Horn-Omni sounder TUW

The structure of the TUW sounder is shown in Fig. 1a. The TX setup includes an AWG that produces a complex baseband signal (details will be discussed below). This baseband signal is then up-converted and amplified by an external mixer module to achieve a center frequency of 60 GHz. The obtained RF signal is transmitted through a 20 dBi gain conical horn antenna with an 18° half power beam width (HPBW).

On the RX side, the signal is captured by a custom-built omnidirectional $\lambda/4$ monopole antenna. The received signal is then processed by a signal analyzer that can work directly with the RF signal, i.e., does not need any external down-converters. In order to enhance the SNR, coherent averaging over N_{rep} (contiguous) repetitions of the sounding sequence is used. To achieve accurate frequency synchronization, all RF devices at both the transmitter and receiver use a 10 MHz reference signal. For time synchronization, the measurement begins the moment the moving vehicle crosses a light barrier, which triggers the recording at the receiver.

The sounding signal is a multi-tone sounding signal based on a modified Zadoff-Chu sequence that ensures a low PAPR (see [57]). For the parameters of this signal we used two different configurations depending on the measurement scenario. For the overtaking scenario, 121 subcarriers with a spacing of 4.96 MHz were used, and $N_{\mathrm{rep}} = 640$ is used for the evaluation, resulting in the bandwidth, maximum excess delay, and maximum unambiguous Doppler listed as the first set of numbers in column 2 of Table 1. The receiver's memory, with a depth of approximately 420 MSamples, allows for capturing up to 720 ms of channel evolution at a sampling rate of 600 MSamples/s.

For the V2I measurements, only 21 subcarriers with a subcarrier spacing of 4.76 MHz are used, and $N_{\mathrm{rep}} = 212$ is chosen, resulting in the bandwidth, maximum delay and maximum Doppler listed as the second numbers in column 2 of Table I. Additionally, this scenario involves two simultaneous TXs. To measure the channel for both TXs simultaneously, a frequency division multiplexing technique is employed. Specifically, the multitone waveform for the second TX is created by applying a 1.19 MHz frequency offset to each tone of the first TX, resulting in orthogonality between the waveforms from the two TXs. For a chosen sampling rate of 125 MSamples/s, the recording time is 3.6 s, resulting in a travel distance of 50.4 m.

In either case, the calibration function $H_{\mathrm{sounder}}(t, f)$, is obtained from back-to-back measurements, thus excluding the antennas. The use of the calibration function will be discussed in Sec. V.A.

During the V2V measurements, the TX was mounted on a tripod and the RX was in a Mazda 5 car. During the V2I measurement, the TX was on the roof of a car, while the RX was at the location of the roadside unit (RSU).

TABLE 1. Key parameters of the sounders. MT...multitone. 0 GHz for the IF means generation of complex BB signal.

Sounder	TUW (V2V/V2I)	BUT	AIT	USC
Carrier freq [GHz]	60	59.6	3.2, 34.3, 63.35	60.4
bandwidth (BW) [GHz]	0.51/0.1	4.0	0.16	0.2
max PA power [dBm]	7	23	10	22
sounding seq	MT	Golay	MT	MT
max delay [m]	60/63	49.13	600	600
max Doppler [kHz]	3.9/2.8	2.5	16	N/A
IF [GHz]	N/A	N/A	direct, 29, 59	0.3/3.7
Digitizer ENOB	N/A	5.2	N/A	6
max recoding time [s]	0.72/3.6	0.18/0.93/4.6	unlimited	unlimited
TX ant (type/gain)	horn, 18 deg	omni	omni	horn, 25 deg, 17 dB gain
RX ant (type/gain)	omni	omni/horn 6.2 deg, 32 dB gain	horn 18 deg, 20 dB gain	horn, 9 deg, 25 dB gain

TABLE 2. Components used in the sounders.

Sounder	TUW	BUT	AIT	USC
Signal generator	Keysight M8195A	Anritsu MP1800A	NI USRP-2954R	Keysight N8241A
Freq synth	R&S SMA100A	Agilent 83752A	Anritsu, MXG, Agilent MG3690B, N5183B, 83752A	NI, Mercry quickSyn, DS-3002
Mixer/upconv	Pasternack PEM001	SiversIma FC1005V/00	Marki, SiversIma ADA2050, FC1005V + FC1003V	Spacek labs T60-14.25 and M60-5
PA	N/A	Quinstar QPW-50662330-C1	Cernex, Quinstar CBM18402023, QPW-50662330-C1	Eravant SBP-5536533022-1515-E1
LNA	N/A	Quinstar QLW-50754530-I2	Cernex, Quinstar CBLU 20403575, QLW-50754530-I2	Eravant SBL-5037533550-1515-E1
Digitizer	R&S FSW67	Tektronix MSO72004C	NI USRP-2954R	NI PXIe-5162
Clock	SRS FS725	Datum LPRO 10 MHz	GPS10eR	Jackson Labs LN Rubidium

B. Omni-Omni/horn sounder BUT

The BUT sounder is a time-domain spread spectrum channel sounder whose block diagram is shown in Fig. 1b (for details see [13]). The sounding sequence is a seamlessly repeating pair of Golay complementary sequences, operating at the data rate of 12.5 Gbit/s. They are generated by an Anritsu Signal Quality Analyzer, then frequency limited to the 0 – 4 GHz band by a low-pass filter (LPF), upconverted into the mmWave band, and amplified. The received signal passes through an LNA into a quadrature down-conversion mixer, which produces the complex baseband signal that is digitized and stored in a Tektronix Mixed Signal Oscilloscope (20 GHz, 50 GS/s) working as a matched receiver. The TX and RX are synchronized by a Rb-disciplined oscillator.

The Golay complementary pair consisting of 2×2048 bits is combined with the inverted counterparts (another 2×2048 bits); this is done to suppress spurs that decrease the dynamic range produced by nonlinear behavior of the PA, LNA and mixers [14]. Each sequence is sent twice to facilitate channel estimation in the presence of multipath propagation, i.e. a recurring sequence of 8×2048 bits (two repetitions of the complementary pair and its inversion), is used for channel sounding. The real dynamic range is about 45 dB. The maximum observable delay is 163.8 ns, which corresponds to a distance of 49.13 m, and the number of stored CIRs acquired at selectable intervals can be up to 932.

During the V2V and V2I measurement campaigns two identical omnidirectional substrate integrated waveguide (SIW) slot antennas and one horn antenna were used. The omnidirectional antennas were designed and implemented at BUT specifically for channel characterization [58]. The use of different natural resonant frequencies of the narrow-band slots ensures a relatively wide operating frequency band (55-65 GHz), but on the other hand, such a relatively

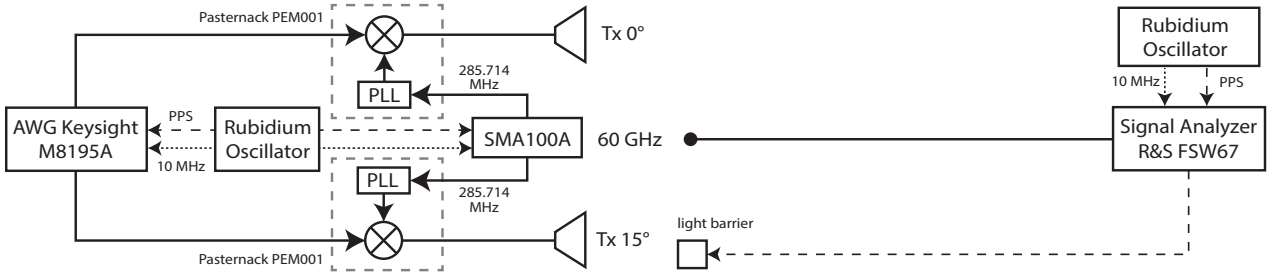

(a) TUW channel sounder (60 GHz).

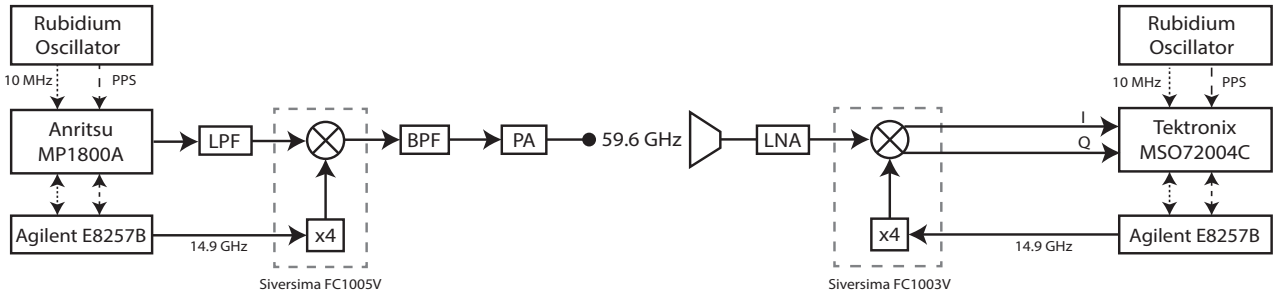

(b) BUT channel sounder (59.6 GHz).

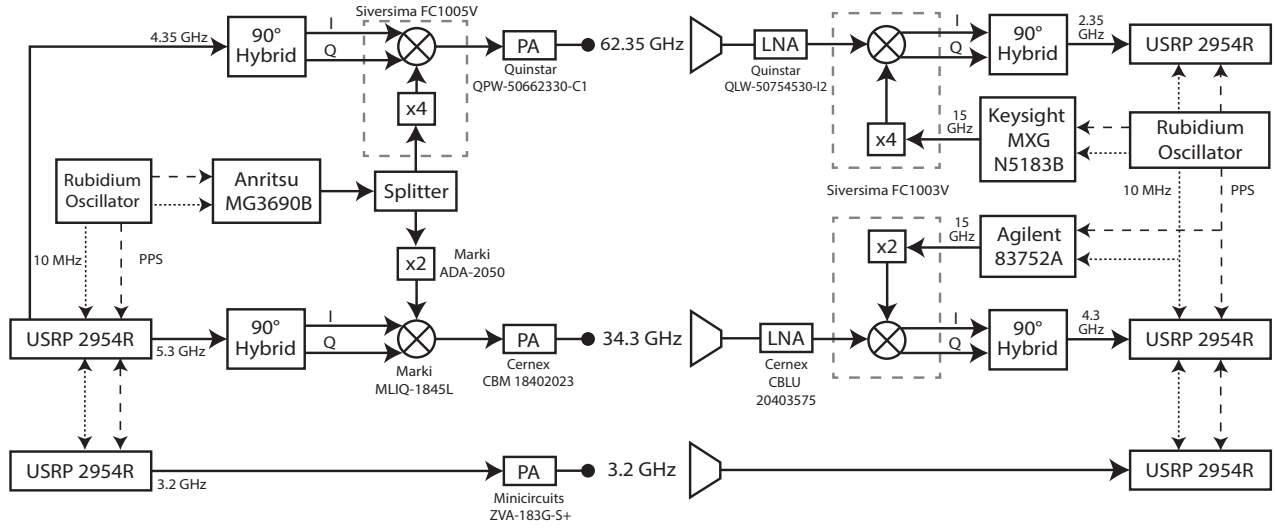

(c) AIT channel sounder (3.2 GHz, 34.3 GHz and 62.35 GHz).

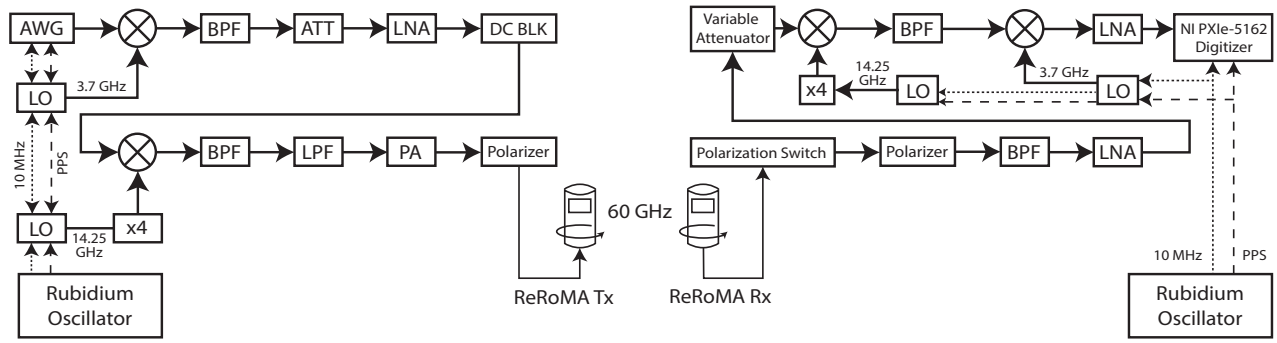

(d) USC channel sounder (60 GHz).

FIGURE 1. **Block diagrams of channel sounders used in this study.**

FIGURE 2. Measurement setup and environment of the opposite-lane passing V2V measurements at BUT.

broad frequency range exhibits a non-negligible variation in gain from -7 dB to 5 dB (relative to a mean value of 0 dBi) depending on frequency and horizontal radiation angle. The signal during the V2I measurements was received using a custom-made horn antenna with a dielectric lens manufactured by Flan company.

During calibration, the PA output waveguide is connected to the LNA input waveguide via a 60 dB attenuator. First the IQ imbalances are compensated and then the sounder transfer function required for CTF calculation is measured. Because only one of the IQ inputs is used in the up-converter at the TX side, the IQ imbalance is a concern only at the RX side. Several hundred CIRs $\hat{h}_i(\tau)$ are measured, where $i = 1, 2, \ldots, N$ denotes the i-th measurement. We then model the CTF $\hat{H}_i(f) = \mathcal{F}[h_i(\tau)]$, affected by the IQ imbalances, as $\hat{H}_i(f) = H_i(f) + k(f)H_i(-f)$, where $H_i(f)$ is the complex baseband representation of the CTF without the effects caused by IQ imbalance, and $k(f)$ is the complex frequency dependent IQ imbalance coefficient, and for every frequency bin f, such value of $k(f)$ is found that the resulting trace of $\hat{H}(f)$ in the complex plane fits a circle best in the least squares sense. In the next step we perform a back-to-back calibration (which excludes the antennas) and measure the sounder transfer function $H_{\text{sounder}}(f)$.

During the V2V measurements, two cars, a (Volkswagen (VW) CC 2.0 TDi and a Ford Fusion 1.4i) carry the TX and RX parts of the sounder as shown in Fig. 2. Due to large power consumption of the oscilloscope the RX part was supplied from a power station carried on a trailer. During the V2I measurements, the TX was in the VW and the RX was at the RSU location.

Remark 1 The BUT sounder was recently updated. In this new version, the Anritsu generator and oscilloscope are replaced by Zynq UltraScale+ RFsystem on chip (SoC) development kits with 12-bit 4.096 GSps ADCs and 14-bit 6.554 Gsps DACs, the rubidium oscillators are replaced by

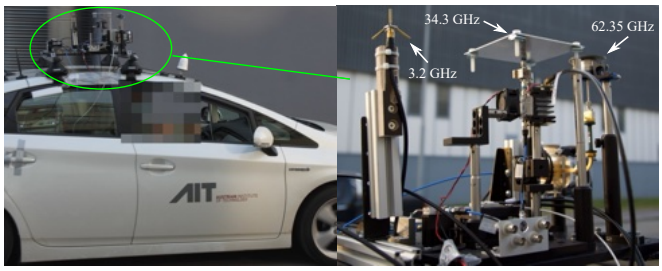

FIGURE 3. TX antenna of the AIT sounder mounted on car rooftop, from [2].

SRS GPS Frequency & Systems FS740, and the Agilent signal generators are replaced by Simon TFS21-22-200 Low Phase Noise Frequency Synthesizers. The channel sounder is now capable of simultaneous measurements in the 60 and 80 GHz bands with 2 GHz bandwidth using frequency modulation. However, the measurements reported in this paper use the old setup.

C. Multiband Horn-omni sounder AIT

The AIT sounder, depicted in Fig. 1c has as its most distinctive feature the ability to perform channel sounding measurements simultaneously at 3.2 GHz, 34.3 GHz and 62.35 GHz to obtain the time-variant CTF $H_i(t, f)$, where i indicates the frequency band. In order to make the results comparable across frequency bands, we use vertically polarized antennas with comparable patterns, namely a donut-shaped omni-directional pattern at the TX and a directional pattern at the RX.

Fig. 1c depicts the TX on the left side. Two National Instruments (NI) USRP SDRs [59] generate multitone based sounding signals, whose detailed parameters are presented in Tab. 1. Each up-conversion stage uses 90°-hybrid couplers to convert the IF signal to I/Q signals. The USRPs are controlled by an NI PXIe-1082. Synchronization and triggering is performed via a Rubidium clock. Fig. 3 depicts the custom-built omni-directional monopole TX antennas. The detailed antenna properties can be found in [2].

In Fig. 1c the RX is shown on the right side. Three USRPs record the received sounding signals at the three frequency bands simultaneously. A redundant array of independent disks (RAID) stores the measurement data. The directional RX antennas are mounted on a tripod as shown in Fig. 4.

At TX and RX, Precision Test Systems GPS10eR Rb clocks provide a 10 MHz reference signal with low phase noise and a 1-pulse per second (PPS) signal for timing synchronization between TX and RX. Before the measurement starts, the RX Rb clock is connected via coaxial cables to the TX Rb clock (which acts as primary clock source) and disciplined. After synchronization of about one hour and after a calibration measurement, the Rb clocks are separated and both clocks are set to free-run mode [60].

To calibrate the multiband channel sounder, a back-to-back calibration measurement is performed for each RF chain (i.e.,

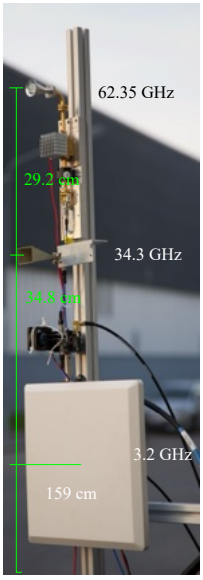

FIGURE 4. RX antennas of the AIT multiband sounder mounted on a pole of a tripod, from [2].

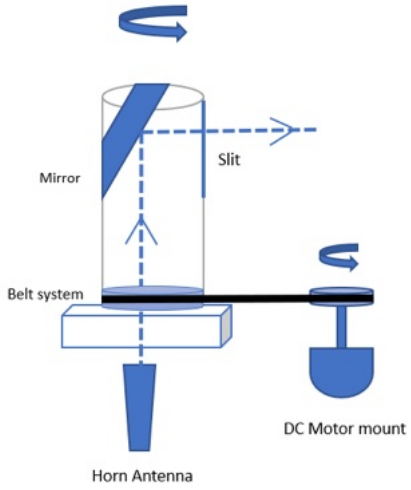

FIGURE 5. ReRoMA sample configuration diagram. From [6].

frequency band). In this process, the TX and the RX of each chain are directly connected using attenuators and the CTFs are recorded.

During the V2V measurements, the TX antenna was on the rooftop of a Mitsubishi i-MiEV, and the RX on a Toyota Prius. During the V2I measurements, the TX was on a Toyota Prius, and the RX at the RSU location on the pavement of the street.

D. ReRoMA

The USC sounder, shown in Fig. 1d differs from the other sounders in the consortium in that it provides directional resolution at both link ends. It achieves this by combining a SISO channel sounder with horn antennas with a mechanical contraption that re-directs the beams in a time-variant way. This patent-pending approach [61] designed in collaboration between USC and TUW, called ReRoMA combines the simplicity of traditional rotating-horn setups with the ability to measure dynamic channels.

The SISO channel sounder follows the principles outlined at the beginning of Sec. III. A low-IF real sounding signal is generated by an AWG. The multi-tone sounding signal is a variation of a Zadoff-Chu signal that provides better PAPR when oversampled and filtered. The signal is then upconverted in two stages, amplified, and a single sideband is filtered out through a band-pass filter (BPF). Transmission occurs with a left hand circular polarization (LHCP), through an antenna with $25\,\mathrm{deg}$ beamwidth. At the RX, the signal is sensed by a horn antenna with $9\,\mathrm{deg}$ beamwidth (the reason for the different beamwidths will be discussed below). The output of the horn antenna first goes through a polarization switch, so that alternating repetitions of the sounding sequence are received with LHCP and right hand circular polarization (RHCP), respectively. The signal is downconverted in two stages to a 300 MHz IF. Variable amplification provides a dynamic range of 45 dB. The real IF signal is sampled by a digitizer, and results are streamed to a RAID for storage and later postprocessing. The relatively low signal bandwidth of 200 MHz and signal repetition frequency of 200 μs is mainly due to the limitations of the NI digitizer, in particular the low speed at which it allows continuous streaming of data to an external harddisk; on the upside, recordings can be made over extended time periods (more than 30 min).

Synchronization between TX and RX is achieved by means of two GPS-disciplined Rb clocks. The 1PPS signal of the clocks is only used to trigger once, and then for monitoring purposes, in order not to introduce phase jumps associated with re-triggering, which would be detrimental for high resolution parameter estimation (HRPE) of the results in particular if occurring between burst of the same MIMO snapshot.

The directional resolution is achieved by means of a rotating mirror arrangement as sketched in Fig. 5. The basic principle is to separate the rotating mechanical parts from the signal-generating parts of the sounder (up to and including the antennas), as this allows much faster rotation and avoids expensive and failure-prone components such as rotational joints. The horn antenna at the TX is pointed upwards, and the beam emitted by it is redirected by a 45° inclined mirror into the horizontal plane. The mirror is located in a tube, similar to a periscope, which rotates with high speed, driven by a direct current (DC) motor. The position of the tube is not controlled, but rather monitored (by means of an optical encoder). A similar arrangement is placed at the RX. The RX tube rotates with about 2000 rotations per minute (rpm), and thus finishes a full rotation in about 30 ms; the signal (in each polarization) is thus sampled every 5°. The TX mirror rotates much slower, so that it moves only 10° while the RX

FIGURE 6. RX of the ReRoMA sounder loaded on the back of the pickup truck.

FIGURE 7. Map of the V2V convoy measurements at USC. From [7].

performs a full rotation (the beamwidth of the TX is chosen to be about twice this angle difference).

For the calibration, we performed a separate back-to-back calibration of the SISO sounder (separately for the two polarization directions) and a calibration of the antenna pattern of the ReRoMA antenna pattern in the anechoic chamber. This separate calibration is meaningful in this case because the data from the sounder can form the basis of directional HRPE evaluations for which the separate knowledge of the antenna patterns and back-to-back calibration is essential. A more detailed description of the ReRoMA principle, as well as calibration and test measurements, can be found in [6].

During the measurement campaign, the TX and RX were loaded onto the beds of two pickup trucks, model Chevrolet Silverado. The mirrors were high enough as to not be obstructed by the driver cabin, so that full 360° field of view was provided as shown in Fig. 6. In addition to the sounder itself, equipment to capture location and speed of the vehicle, as well as 360° cameras were mounted on the trucks; this is useful in the interpretation of the data during postprocessing.

IV. Measurement Scenarios

A. V2V

1) Convoy

The convoy measurements of USC were done within the University Park Campus in downtown Los Angeles, as shown in Fig. 7. There is a stretch of road that is abutted by open areas (sports field, etc.). The rest of the streets are lined with buildings of mostly medium height, 3-5 storeys. There are spacings between the buildings, making the environments somewhat different from ”traditional” downtown environments (i.e., buildings flush with each other). At some sections of the road, cars and trucks were parked, as can be expected in an urban environment. The distance between the two cars in the convoys was mostly 10-15 m (except when stopping at intersections); no blocking vehicles were included in the experiments.

2) Opposite lane passing

USC: For the scenario in which the cars drive in opposite directions and pass each other (henceforth called opposite-lane passing lane), USC performed measurements on a major thoroughfare in downtown Los Angeles, namely Vermont Avenue. This street has 6 lanes (two of which serve mainly for parking, with trees and bushes on the sidewalks, and low-rise buildings (with gaps in between them) beyond the sidewalks. Measurements were done on a stretch of road of a length of approximately 350 m, and vehicles drove with essentially constant speed of about 15 km/h.

BUT: The opposite-lane measurements of BUT took place on the campus of the Faculty of Electrical Engineering and Communication Technologies of Brno University of Technology between the building at 12 TechnickÃ¡ Street and the faculty parking lot (garage) (see Fig. 2 and https://en.mapy.cz/s/gozunovaje). Only lighting columns, traffic signs, medium sized trees, and a low wall bordering the parking lot are in the vicinity of the road within the measurement range. The wall is divided by two 3 m long metal barriers. The width of the road is about 6 m and the sidewalks on both sides are 2 m wide. The wall is 1.2 m high, 7 m long and its distance from the road is about 6.5 m. The omnidirectional antennas along with the outdoor units were mounted to the roof and window of the vehicles.

3) V2V overtaking

TUW conducted measurements of 60 GHz V2V channel realizations to study the impact of an overtaking vehicle. The experiment was inspired by a scenario where two cars - a transmitter car and a receiver car - maintain a constant distance of 15 m while communicating via a 60 GHz mmWave link (see Fig. 8). A third vehicle, traveling at speeds of up to 13 m/s, overtakes the two-car platoon, thereby affecting the wireless channel. To simplify the measurements, the TX and RX cars are kept static, with the overtaking vehicle simulated by regular street traffic. In the setup, the TX

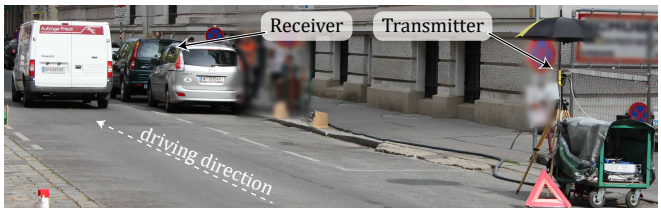

FIGURE 8. **Measurement setup and environment for the V2V overtaking measurements of TUW. TX and RX are fixed at a distance of 15 m apart, while the wireless channel is influenced by an overtaking vehicle.**

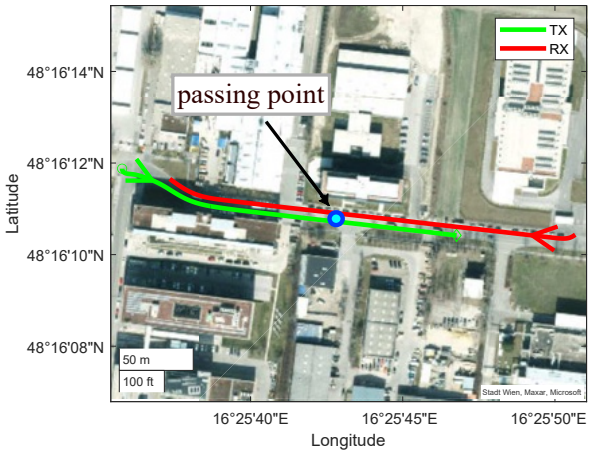

FIGURE 9. **Measurement setup and environment for the V2V opposite-lane passing measurements of AIT. TX and RX pass each other at the indicated passing point, see [3].**

car used a horn antenna directed towards the receiver car, while the receiver car was equipped with a custom-built omnidirectional monopole antenna mounted on the left rear window. Measurements were performed in Gusshausstrasse in downtown Vienna. The street is abutted by contiguous 5-story buildings (about 20 m height) on both sides. In addition to the sidewalks, the street contains 4 lanes, two of which are occupied by parked cars; the total width of the street is 20 m.

USC measured for a somewhat different scenario involving only two cars - one was parked on the side of the street, and the other passed it. The location of these measurements was Vermont Avenue, which is described in Sec. IV.A.1. The wide street, ample vegetation, and low building density led to a paucity of reflected MPCs, as elaborated more in Sec. V.C.

AIT conducted dual band channel measurements for a V2V overtaking scenario. This scenario is also a two-car scenario, where the TX car equipped with an omni-directional antenna, passes a RX car with a directional horn-antenna. Measurements are done in an urban environment that is characterized by mostly industrial buildings (Giefinggasse) as depicted in Fig. 9, see [3]. The street is approximately 10 m wide, with 3-5 storey buildings on both sides. Ten repetitions are performed for the measurement; the duration of one measurement run is 30 s.

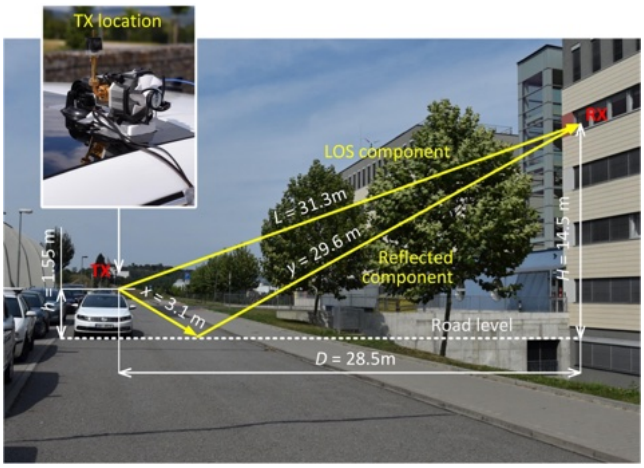

FIGURE 10. **V2I Measurement setup and environment for the V2I passing measurements of BUT. The distances correspond to the situation where the car is closest (in the left lane) to the RX.**

B. V2I

BUT: The V2I measurements of BUT were performed on the BUT campus between the building at Technicka 12 street and a VW CC car driving on the road in front of the building as shown in Fig. 10 and https://en.mapy.cz/s/cuzasaheko). The road is the same as described above, i.e. it is 6 m wide with 2 m of sidewalks on both sides. The RSU is placed in a window opening on the 6th floor of a building, at 14.5 m above ground (the building is 21.5 m high) and the trees are about 6 m tall. The car was moving in both directions (right-to-left as shown in Fig. 10 and left-to-right) at different speeds from v = 30 km/h to 50 km/h. Note that for left-to-right, D = 25 m (because the car goes on the roadside closer to the RX) and L = 28 m. The TX was situated in the car and its SIW slot antenna together with the power amplifier and cooler were placed on the car roof as shown in Fig. 10. The RX horn antenna was mounted on a photographic gimbal head and tripod and directed out of an open window. The antenna was manually directed to the moving car using a riflescope. The correctness of the RX antenna alignment during the tracking was checked using a video recorded by a camera mechanically coupled to the antenna. For all the car speeds and directions, we had performed three measurements and then selected the measurement where the car tracking was the most accurate. Overall, the selected measurements exhibit vertical and horizontal errors of less than 2° and 3° respectively, which causes variations of the horn antenna gain up to 2-3 dB depending on frequency.

TUW conducted V2I channel measurements in an urban street intersection scenario, with the particular goal of evaluating beam diversity on the car. Measurements were done in Gusshausstrasse, which was described in Sec. IV.A.3. Specifically, a vehicle equipped with two horn transmit antennas mounted on its roof rack drove through the street canyon, approach (and crossing) an intersection, see Fig. 11. Both horn antennas were aligned in the direction of travel,

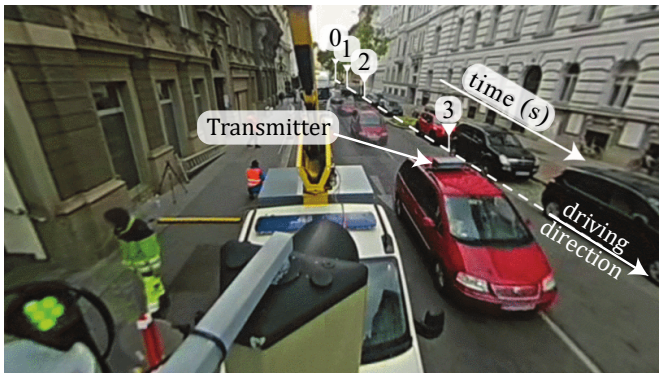

FIGURE 11. Measurement setup and environment for the V2I passing measurements of TUW as seen from the RX. A vehicle with two TXhorn antennas approaches and crosses the intersection within a street canyon, cf. [8].

aimed towards the intersection. One antenna emitted a beam at an elevation angle of 0°, while the other emitted at an elevation angle of 15°. This setup was selected to evaluate how different beam elevation angles affect the characteristics of the V2I communication channel. The RX, equipped with an omnidirectional monopole antenna, was positioned on a crane arm 5 m above the intersection, representing equipment mounted on a traffic light. As the vehicle passed through a light barrier, it triggered the receiver to start recording. Each measurement lasted for 3.6 s and began when the vehicle was either 24.5 m or 40.95 m away from the RX antenna.

AIT: The V2I measurements of AIT were designed specifically to evaluate correlations between different frequency bands, namely 3, 34, and 63 GHz [2]. A TX car moves on an urban streettowards a "T"-intersection and stops. The RX is stationary and is equipped with three directional antennas arranged vertically on a tripod, see Fig. 4. It is placed adjacent to an office building on the pavement 1.5m above street level. The TX is equipped with three omni-directional antennas mounted on the rooftop (see Fig. 3) of the vehicle. Measurements were done in the same industrial urban environment (Giefinggasse) as described in Sec. IV.A.3. The car travels past the RX and stops at a road intersection. The TX trajectory, the RX position and the orientation of the directive antennas are depicted in Fig. 12.

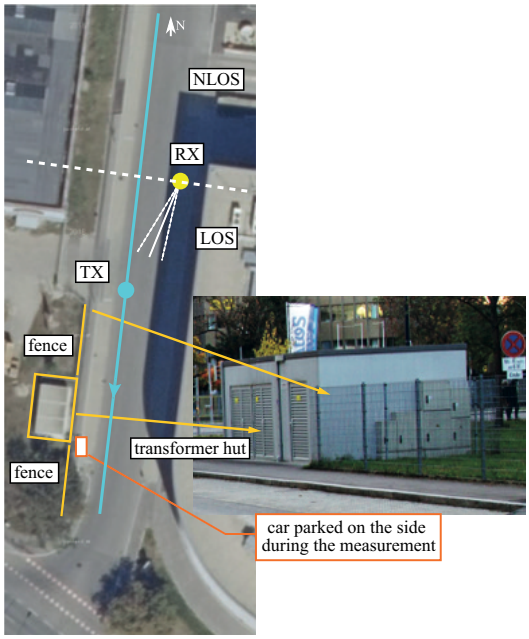

FIGURE 12. Measurement setup and environment for the V2I passing measurements of AIT. [2, Fig. 6]. A TX car approaches a "T"-intersection and stops. The directive RX horn antennas are pointed towards the road intersection. On the right side of the road there is a metallic fence with metallic pillars and a transformer hut.

V. Evaluation Procedure

A. Fourier evaluations

Most of the measurements are processed by Fourier evaluation, because of the simplicity of the method which therefore eases processing of large amounts of measurement data. The processing steps are fairly standard but repeated here for the convenience of the reader. The starting point is either a measured time-variant CTF $H(t, f)$ or its corresponding CIR $h(t, \tau)$; which of those is available depends on the chosen sounding sequence: PN sequences provide the CIR in a straightforward way, while multi-tone sequences give the CTF, see also Sec. III. In any case, conversion between these two representations is easily done through a discrete Fourier transform (DFT). The first step is to calibrate out the system response of the channel sounder. This is most easily achieved in the frequency domain, providing $H_{\text{chan}}(t, f) = H_{\text{meas}}(t, f)/H_{\text{sounder}}(t, f)$ within the band of interest. While such a zero-forcing approach can lead to some noise enhancement, it is typically negligible in the band of interest; otherwise a minimum mean square error (MMSE) approach can replace the zero forcing.

The calibrated CTF can then be filtered in the frequency domain to reduce sidelobes in the delay domain, with the choice of the filter representing a compromise between sidelobe level and SNR variation in the frequency domain. A noise thresholding of the resulting impulse response is then implemented, where the threshold level can be chosen either as a constant level above the measured noise floor, or to maintain a fixed dynamic range. While most of the measurement evaluations use the former approach, the latter approach was chosen for the multiband measurements, in order to have a fair comparison of delay spread and other characteristics between the bands of interest. More details about how to choose thresholds and implement potential delay gating for noise reduction can be found in [62].

The delay-Doppler profile (spreading function) is then computed from the short time Fourier transform with respect to t, i.e., $s(t'; \nu, \tau) = \mathcal{F}_t\{h(t, \tau)\}$ for the interval $t \in (t', t' + T)$. Since the Doppler is changing over time, the Fourier transform has to be applied with respect to a

(sliding) window whose length T must be shorter than the stationarity time of the channel; this will be discussed below in more detail.

From the impulse response or spreading function, we can then compute other parameters that are suitable for a compact representation of the channel; note that in many cases we use the known (e.g., via GPS) distance between TX and RX as function of time to map the time-dependent quantities onto distance-dependent quantities. The instantaneous PDP is $P_h(t,\tau) = |h(t,\tau)|^2$. The path gain is computed as $PG(t) = \int P_h(t,\tau)\mathrm{d}\tau$.

B. Local scattering function

In both V2V and V2I channels, the assumption of stationarity, i.e., that the statistics of the channel are time-invariant, holds only for a limited time windows with length T. Thus, for measurement evaluations, the local scattering function (LSF)

$$\hat{\mathcal{C}}(t',\nu,\tau) = \frac{1}{IJ}\sum_{w=0}^{IJ-1}\left|\mathcal{H}^{(G_w)}(t';\nu,\tau)\right|^2. \quad (1)$$

is utilized to further reduce the noise variance (with a minor increase of the estimation bias, see [63]). The $\mathcal{H}^{(G_w)}(t';\nu,\tau)$ is related to the windowed frequency response as

$$\mathcal{H}^{(G_w)}(t';\nu,\tau) = \int_{-B/2}^{B/2}\int_{t'}^{t'+T} H(t,f) \cdot G_w(t,f)\mathrm{e}^{-\mathrm{j}2\pi(\nu t-\tau f)}dtdf\,, \quad (2)$$

where the measurement bandwidth is denoted by B, and the $G_w(t,f)$ are tapering functions. The best choice of the stationarity region length T is still under investigation. Hence, different parameterization have been used by different groups:

- *AIT:* The tapers $G_w(t,f)$ are two-dimensional prolate spheroidal wave functions [63]. The number of tapers in the time and frequency domain is set to $I = 2$ and $J = 1$, respectively. The stationarity duration is chosen as $T = 100\,\mathrm{ms}$. For a a velocity of $v = 10\,\mathrm{m/s}$ the spatial stationarity length $Tv = 1\,\mathrm{m/s}$, i.e., $\{10.7, 114.3, 207.3\}$ wavelengths at $\{3.2, 34.3, 62.35\}$ GHz.
- *TUW:* Same setup as for AIT, but for the V2V and V2I measurements, $T = 30\,\mathrm{ms}$ and $T = 46\,\mathrm{ms}$ are used, respectively.
- *USC:* A rectangular taper of duration $T = 1.024\,\mathrm{s}$ is used, i.e., the scattering function with as single rectangular taper simplifies to the absolute value squared of the spreading function, $\hat{\mathcal{C}}(t',\nu,\tau) = |s(t';\nu,\tau)|^2$.

We calculate the PDP and Doppler spectral density (DSD) as the expectation of the LSF over the Doppler domain or the delay domain, respectively:

$$\hat{\mathcal{P}}_\tau(t';\tau) = \frac{1}{T}\int \hat{\mathcal{C}}(t';\nu,\tau)d\nu, \quad (3)$$

$$\hat{\mathcal{P}}_\nu(t';\nu) = \frac{1}{B}\int \hat{\mathcal{C}}(t';\nu,\tau)d\tau. \quad (4)$$

For the multiband measurements, to allow for a better comparability between different frequency bands we normalize the Doppler shifts of the DSDs to their respective wavelength obtaining normalized Doppler shifts or velocities

$$v_i = f_{\mathrm{D},i}\lambda_i. \quad (5)$$

The RMS delay spread is the square root of the second central moment of the PDP [64]

$$\sigma_\tau(t) = \left[\frac{\int \hat{\mathcal{P}}_\tau(t;\tau)\tau^2\mathrm{d}\tau}{\int \hat{\mathcal{P}}_\tau(t,\tau)\mathrm{d}\tau} - \left(\frac{\int \hat{\mathcal{P}}_\tau(t,\tau)\tau\mathrm{d}\tau}{\int \hat{\mathcal{P}}_\tau(t,\tau)\mathrm{d}\tau}\right)^2\right]^{1/2}. \quad (6)$$

Please refer to [65] for more details on condensed channel parameters in non-stationary scenarios.

It must be noted that all of these quantities are dependent on the used antennas in the measurements. The exception are the measurements with the double-directional sounder (Sec. III.E), which allow to synthesize PDPs with different antenna patterns; in our evaluations we focused on (i) the omnidirectional PDP (i.e., synthesized in such as way that it is approximately equal to the PDP that would be measured with an omnidirectional antenna,[1] and (ii) the max-dir PDP, i.e., the PDP seen when the horns at TX and RX are oriented such that they provide maximum power.

C. Cosine similarity

To analyze the similarity between frequency bands in the multi-band measurements of AIT, the correlation, i.e. the cosine similarity, of the LSF between different frequency bands is computed according to

$$\rho_{i,j}(t') = \frac{\int\int \mathcal{C}_i(t';\nu,\tau)\mathcal{C}_j(t';\nu,\tau)d\nu d\tau}{TB\sqrt{\sigma_i^2\sigma_j^2}}, \quad (7)$$

where $i,j \in \{1,2,3\}$ indicate the three frequency bands centered at $\{3.2, 34.3, 62.35\}$GHz. The discrete time expressions for sampled data can be found in [4].

VI. Results

The results collected during the measurement campaigns can be divided into two categories: (i) sample results where the peaks in the time-variant PDP can be assigned to reflection/scattering from particular environmental objects, thus giving insights into the dominant propagation mechanisms, and (ii) statistics of the condensed channel parameters such as pathloss and RMS delay spread. In the following, we will present these types of results separately for the different scenarios.

[1]The details of the algorithm for synthesizing this profile from the directional measurements is described in [7].

TABLE 3. Channel characteristics estimated from measurements in various scenarios. C:Convoy, O:Overtaking, P:Opposite lanes passing. Note the discussion of the USC stationarity times in Sec. VI.A

V2X scenario	C V2V	P V2V	P V2V	P V2V	O V2V	O V2I	O V2I	O V2I
channel sounder	USC	BUT	USC	TUW	USC	BUT	TUW	AIT
PL coeff. LOS	1.91	N/A	1.89	N/A	1.89	N/A	N/A	N/A
RMS delay spread mean [dBs]	-73.2	-72.6	-78.4	-80.7	-78.3	-82.8	-73.7	-75.4, -77.5, -77.3
RMS delay spread std [dB]	3.05	0.94	2.08	0.11	2.15	5.25	1.35	1, 1, 0.5
stationarity length mean [ms]	17000	147	3000	720	4000	537	1150	N/A
stationarity length std [ms]	4400	150	11000	0	7500	370	1046	N/A
RMS Doppler spread mean [Hz]	N/A	256	N/A	233	N/A	272	417	51, 220, 290
RMS Doppler spread std [Hz]	N/A	62	N/A	31	N/A	38	386	22, 34, 62
angular spread mean	0.06	N/A	0.18	N/A	0.23	N/A	N/A	N/A
angular spread std	0.02	N/A	0.032	N/A	0.021	N/A	N/A	N/A
Window for Doppler [ms]	N/A	186.4	N/A	30	N/A	186.4	46	100
dynamic range for spread calc [dB]	45	45	45	27	45	45	40	35

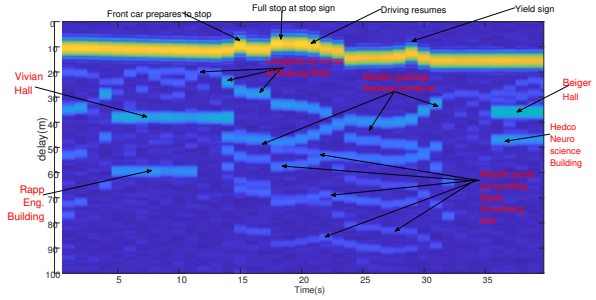

FIGURE 13. Sample time-variant PDP from the V2V convoy measurements. Rapp Engineering Building, Vivian Hall, Beiger Hall, and Hedco Building denote various buildings on the side of the roads the route covered.

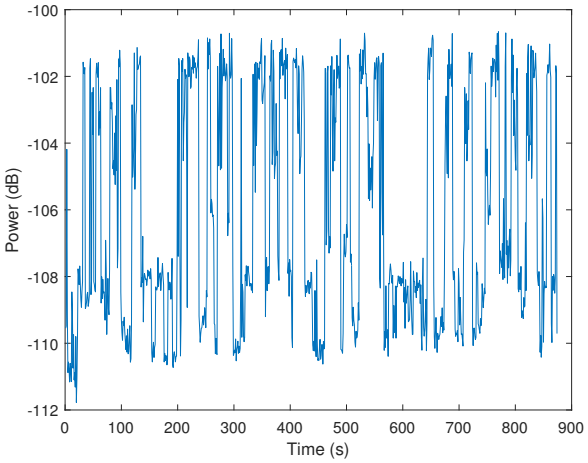

FIGURE 14. Received power (excluding the LOS component) over time in the V2V convoy measurements.

A. V2V Convoy

In the convoy case, PDPs can mainly be separated into two components: (i) the LOS connection, and (ii) potential reflections/scatterings from environmental objects. For the former, it is essential whether the LOS is blocked by objects/other cars. Figure 13 shows a sample omni-directional PDP as a function of time, and indicates with the inserts some of the objects responsible for particular reflections. We can see that both buildings and smaller contributions on the side of the road, such as lampposts and garbage containers, can make contributions of similar strength. Considering the vastly different geometrical sizes, this might be surprising at first glance. However, at the considered small wavelength, even geometrically small objects can lead to strong reflections, though for a shorter period of time.

The reflections from the side are most significant when there are houses and/or parked objects on the side, and reduce at intersections (without stopped cars in the cross streets), and along road stretches bordered by parks of sports fields. Figure 14 shows the received power as a function of time when the LOS delay bin (and the surrounding bins, to reduce the impact of sidelobes) are excluded from the computation of the received power. While the overall received power is dominated by the LOS component, and follows Frii's law quite accurately [7], the power from the other delay bins also shows significant variations. This information can be combined with models for the impact of blockage on the LOS component, as obtained by previous investigations listed in Sec. II. We also note that the strength of the LOS component, compared to the sum of all other components, decreases as the distance between TX and RX increases. However, the changes are not strong, since the distance between the TX and the RX changes only between 4 and 16 m during the measurements.

As shown in Table III, RMS delay spreads are on the order of 80 ns, which might be due to reflections from buildings

that are large yet somewhat farther away because along this route, buildings are set back from the sidewalks. Also note that these are *omni-directional* delay spreads (synthesized as discussed in Sec. V), while the max-dir delay spreads are significantly smaller, with an average around 10 ns. The measurements of the angular spread (computed according to Fleury's definition, which ranges between 0 and 1) show a lower limit of about 0.1 for the TX and 0.05 for the RX, which is due to the different beamwidths of the sounder at the two link ends. The maximum values extend to about 0.25 at the TX and 0.2 at the RX.

The stationarity times strongly depend on two factors: (i) whether considering the omni-directional or the max-dir PDP, and (ii) whether the origin of the delay axis is kept at the transmission time of the signal from the TX, or whether it is adjusted to the arrival time of the LOS component at the RX (as would be done by many practical synchronization algorithms, which synch to the strongest MPC). The former case provides a stationarity time that is mostly determined by how well a constant distance between TX and RX is kept, while the latter case leads to much larger stationarity distances. The max-dir stationarity times in the former case have a median of < 1 s (remember that each MIMO snapshot measurement takes 1 s, so that no stationarity times shorter than 1 s can be measured, while the omnidirectional median is around 5s. Note that similar observations apply to the stationarity times for the USC V2V passing and overtaking measurements.

B. V2V Opposite Lane Passing

BUT: Fig. 15 shows a time-variant CIR for V2V opposite-lane passing measurements on the BUT campus. The total measurement time $T_{\mathrm{TM}} = T_{\mathrm{CM}} \times N_{\mathrm{CIR}}$ was 4.675 s, where N_{CIR} = 932 is the number of saved CIRs per measurement, and $T_{\mathrm{CM}} = 5$ ms is the measurement period of CIRs. The CIR contains a few MPCs reflected from surrounding objects (street lighting columns, traffic signs, trees, and the wall situated on the farther side of the road) and from the car bodies (from roofs and hoods). The significantly decreased level of MPCs reflected from lighting columns, traffic signs and other objects in the case of approaching cars (corresponding to a smaller sampling time) is probably due to their shadowing of components by the taller Ford Fusion. Note that the level of the received MPCs depending on the relative position of the vehicles is also affected by the radiation patterns of the used SIW slot antennas as they exhibit a some variation in gain mentioned in Sec. III. B. The values of the sampling time (delay) are not absolute but rather depend on the time delay between the periodically generated PRBS and the manual triggering of the oscilloscope.

The relative amplitudes of the LOS and the strongest MPC reflected from the surrounding objects (calculated as maximum values for each measurement instant) are shown in Fig. 16a. We see significant power carried by those

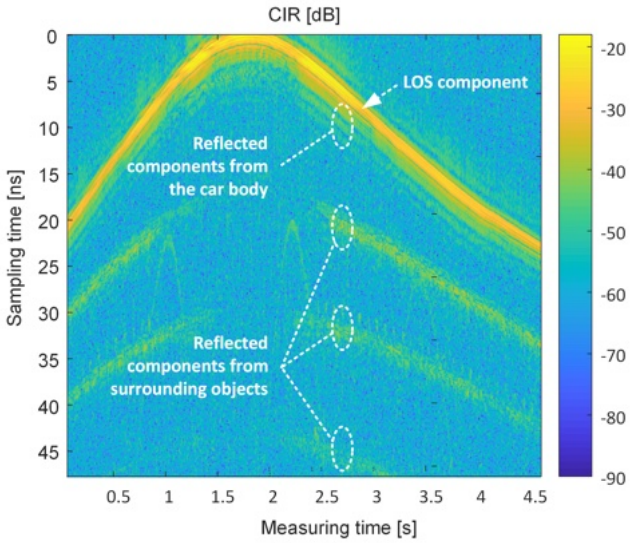

FIGURE 15. Example time-variant CIR for V2V opposite-lane passing measurements on BUT campus.

components, typically 10 dB below the LOS component, indicating that links might be sustained even when the LOS is blocked. The time dependence of the RMS delay spread is shown in Fig. 16b. Its relationship with the amplitude of the LOS component is predictable (the larger the amplitude, the smaller the delay spread). Due to the relatively large power of the reflected MPCs, the RMS delay spread is quite large as shown in Table 3, on the order of more than 50 ns. As we will discuss further below, this value is below the value of the convoy measurements (which had larger buildings abutting the roads) but larger than in the opposite-lane measurements of USC. Note also that while the delay spreads were measured with antennas that are nominally omni, the above-mentioned variations of the gain may impact the results.

We also calculated the RMS Doppler spread for the same scenario. To minimize the limitation of the measurable Doppler frequency we used measurements performed for $T_{\mathrm{CM}} = 0.2$ ms and 1 ms. The averaged values are listed in Table 3.

USC: The USC opposite-lane scenario provides only relatively weak reflected components, due to the wide street scenario described in Sec. IV.B. Since the time-variant PDPs are not very instructive, showing dominantly the LOS component, no examples are shown here. This channel behavior is also reflected in the RMS delay spread, which is significantly lower than in the convoy scenario where the cars drove in an environment with higher buildings that are closer to the street.

AIT: The results of the AIT opposite lane passing scenario show a strong LOS component as well as reflections from a large metallic surface on a building in close vicinity. Furthermore, also some diffuse components can be observed. The corresponding PDP and DSD can be found in [3].

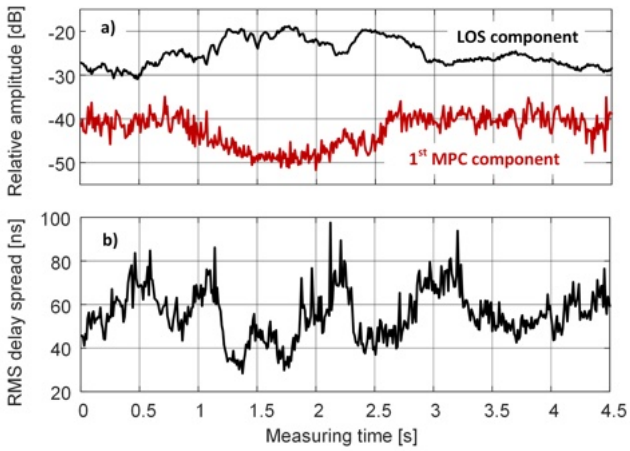

FIGURE 16. **Relative amplitude of the LOS and first MPC component (a) and RMS delay spread (b) in dependence on measuring time.**

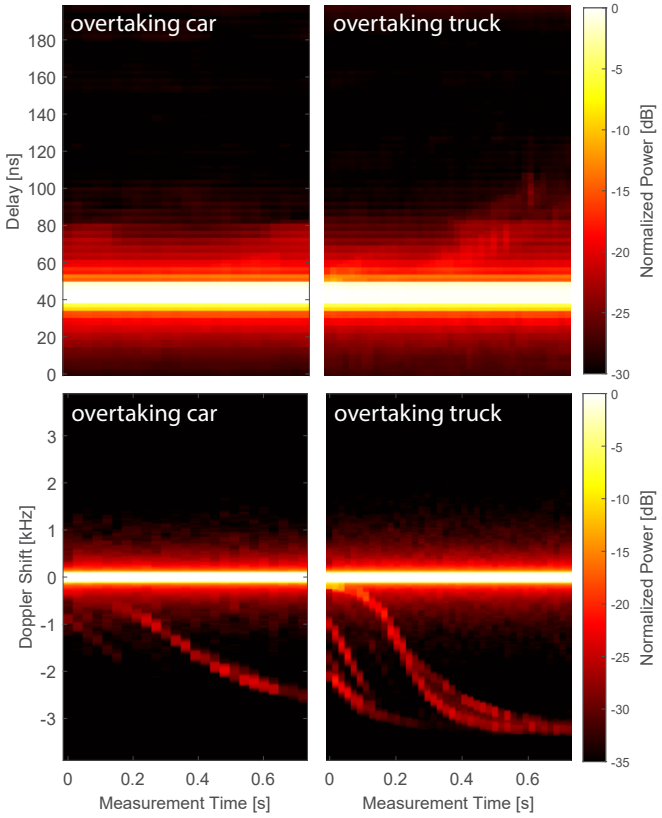

FIGURE 17. **Normalized time-variant PDP (top) and normalized DSD (bottom) with car (left) and truck (right) overtaking the convoy in the TUW V2V overtaking measurements.**

C. V2V Overtaking scenarios

TUW: According to the arrangement described in Sec. IV.C, namely a static TX and RX and temporal dynamics induced by cars overtaking them, we can expect a pronounced static LOS component at a delay of 50 ns, corresponding to a distance of 15 m between TX and RX. This is indeed confirmed in the PDP depicted in Fig. 17. In the DSD, this LOS component appears at a Doppler shift of 0 Hz. The presence of an overtaking car slightly impacts the PDP, but is better visible in the DSD, producing a distinct Doppler trace extending down to a Doppler shift of -2.5 kHz. On the other hand, an overtaking truck significantly influences the PDP. In addition to the static Doppler component at -3 kHz, the truck generates multiple Doppler components. The truck's side walls strongly reflect incoming waves, clearly illustrating its spatial extent compared to the scenario involving the overtaking car.

The RMS delay spread and RX power statistics are not significantly impacted by the passing cars or trucks: e.g., for a passing car, the media delay spread is is 8.83 ns, while for the overtaking truck, it is 8.41 ns (the reduction of the delay spread by a strong reflection can be explained by the fact that the reflection has a short delay (the detour via the moving reflector is small, at least at those times where the reflection is strong), and it thus reduced the delay spread compared to the case where it is dominated by farther-away reflections from building walls. Also note that the delay spreads in this scenario are measured with a horn antenna at one link end, which due to the resulting spatial filtering reduces the delay spread.

On the other hand, the median RMS Doppler spread for the overtaking car is 204 Hz, compared to 251 Hz for the overtaking truck. This indicates that the RMS Doppler spread is significantly influenced by the size of the overtaking vehicle.

USC: In the USC overtaking measurements, strong reflections with considerable delay (30-60 ns compared to the LOS runlength were observed only for part of the measurement time, and could be attributed to some pronounced buildings near the road (compare [7, Fig. 7]). There are also weak components with a delay very similar to that of the LOS; these are mainly cause by vegetation at the boundary of the sidewalk. The angular spreads in this environment are larger than in the opposite-lane measurements performed on the same street, which is related both to the distance distribution (the maximum distance is considerably larger in the opposite-lane scenario), and the objects that can act as effective scatterers during the recording of the impulse responses.

D. V2I Overtaking - BUT

In the V2I measurements on th BUT campus, the RSU used a horn antenna that followed the passing car, as described in Sec. IV. D. This enabled to observe the changes in MPC during a longer time period. The corresponding total measurement time T_{TM} was the same as in the Sec. VI. B.

As shown in Fig. 18, two dominant components (LOS component and first reflected component) were detected when the vehicle was driving on the road. To analyze the MPCs magnitude variation we approximated the coordinates (indices) of direct and first reflected component by a smooth curve plotted in figure.

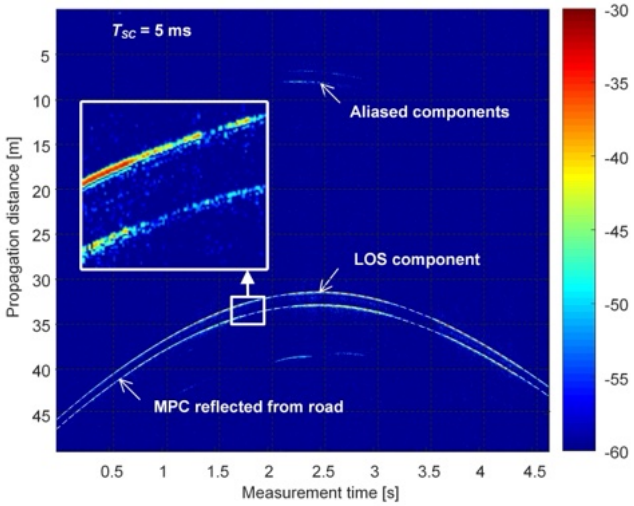

FIGURE 18. Measured CIR magnitude in dBm for velocity v = 40 km/h in the BUT V2I measurements.

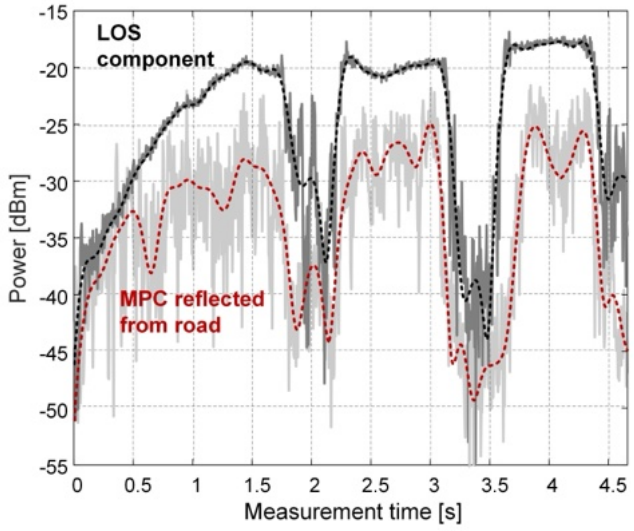

FIGURE 19. The time dependence of the LOS and reflected component magnitudes for v = 40 km/h. in the BUT V2I measurements.

The influence of the trees in Fig. 18 and Fig. 19 is obvious. The attenuation varies over a wide range depending on which part of the tree foliage the mmWave signal penetrates, but can be up to 20-25 dB, which is in line with data in the literature for a canopy of this size. Note that the difference in power between the direct and reflected components is quite small. In the 'unshadowed' segments of the record, the differences in short-term trends are in the range of 6-12 dB. The ripple in the magnitude of the LOS component in the 'unshadowed' areas is probably due to imperfect hand tracking and the angle dependent irradiance of the two antennas. It should also be noted that the parked vehicles were largely shaded by the roof of the passing car and therefore the reflections from them were insignificant.

Finally, we calculated the instantaneous RMS delay spread for the for the LOS component and MPC reflected from the road depicted in Fig. 18 according to (6). The number of taps was chosen experimentally as the number of the CIR peaks exceeding the receiver noise threshold (-60 dBV). The RMS delay spread plotted in the logarithmic vertical scale is shown in Fig. 20. It corresponds well to the magnitudes in Fig. 19. A strong attenuation of the LOS component, and thus a decrease of its power relative to the power of the strongest reflected MPC, obviously causes an increase in the RMS delay spread. Because of the large changes in the LOS component power, the standard deviation of the RMS delay spread (12.7 ns, see Table 3) is also relatively large. The range of averaged values (black dashed waveform) between 2 ns LOS propagation) and 60 ns (shadowing by trees) are typical of outdoor V2X scenarios. We also calculated the RMS Doppler spread in the same manner described in Sec. VI. B.

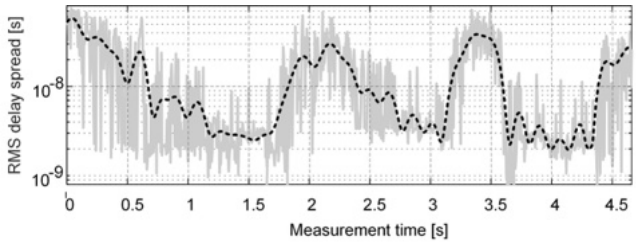

FIGURE 20. The time dependence the instantaneous RMS delay spread for LOS path and v = 40 km/h. in the BUT V2I measurements.

E. Elevation-dependent Diversity "O V2I TUW" scenario

For the "O V2I TUW" scenario in Table 3, the normalized time-variant PDP and DSD for two different TX antenna elevation angles, 0° and 15°, are shown in Figure 21, cf. [8]. The PDP estimates (top) have low resolution in the delay domain, in contrast to the corresponding DSD (bottom).

Each beam contains at least 9 MPCs. As is clearly visible in the DSD, the Doppler spectra are different in the two beams, thus providing a high potential RX diversity order. Due to spatial filtering of the street level, fewer MPCs are observed for the 15° elevated beam. A LOS component with more than 2.5 kHz Doppler shift is visible at 0 s for both TX antenna elevations. The Doppler shift of the LOS component decreases towards negative frequencies as the car approaches the RX due to the corresponding change in radial velocity.

F. V2I Multi-band results - "O I AIT" scenario

The purpose of the AIT V2I measurements was mainly the comparison of the channels in the different frequency bands. The normalized time-variant PDPs are shown in Figure 22. The directional antennas are pointing towards the road intersection, hence only little energy contribution is observed within the first 10 seconds of the measurement. A comparison of the PDPs reveals similar structures in all three frequency bands. Specifically, e.g., the line-of-sight component is clearly visible.

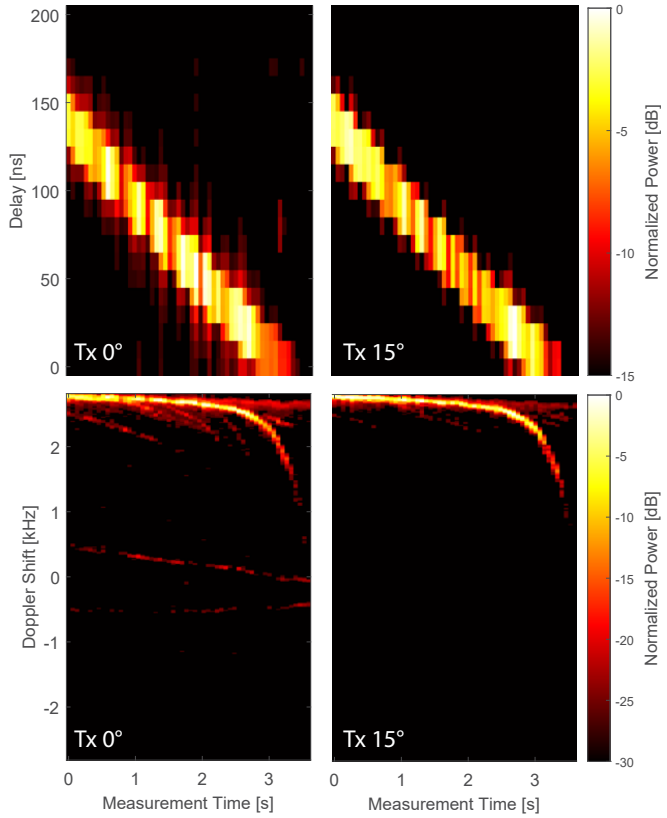

FIGURE 21. Normalized time-variant PDP (top) and DSD (bottom) with TX elevation angles of 0° (left) and 15° (right) in the O V2I TUW scenario with the car approaching the RX at road intersection, cf. [8].

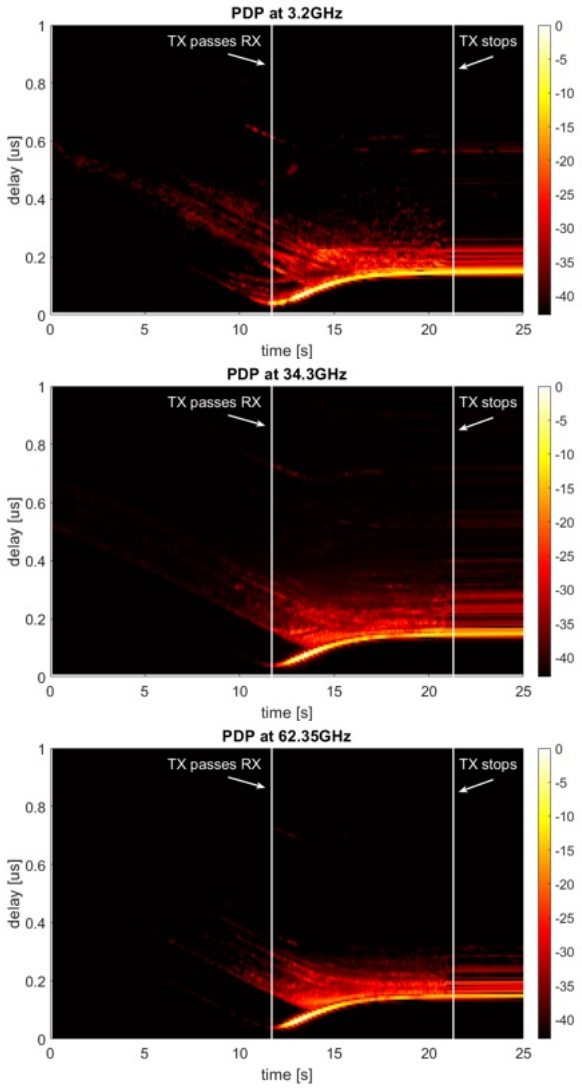

FIGURE 22. PDP for 3.2 GHz (top), 34.3 GHz (middle), and 62.35 GHz band in the AIT V2I measurements, from [2].

In Fig. 23 we show the empirically calculated cumulative density functions (CDFs) of the cosine similarity during the LOS region of our measurement. Different stationarity region lengths are shown for the cosine similarity between the 3.2 GHz and the 62.35 GHz band. From the results we observe that the cosine similarity increases with increasing stationarity region length up to a approximately $10\,\lambda$. Here, the wavelength refers to the 62.35 GHz band. This result can be explained since with increasing observation duration T, the Doppler estimation error decreases. If the stationarity region length Tv is increased above $10\,\lambda$ the cosine similarity decreases again since the stationarity conditions are violated due to vehicular motion.

We show the evaluation of the delay and Doppler spread values for the time-span after passing the RX and stopping at the crossing (time span from 13s to 21s, similar as is used for the evaluation in [4]) in Tab. 3. The mean delay spread was found to be $\{38, 24, 25\}$ ns for the three bands at $\{3.2, 24.3, 63.35\}$ GHz. The standard deviation varies between 9-11 ns between these three bands. For the Doppler spread we found mean values of $\{51, 220, 290\}$ Hz and a standard deviation of $\{22, 34, 62\}$ Hz for the three bands investigated.

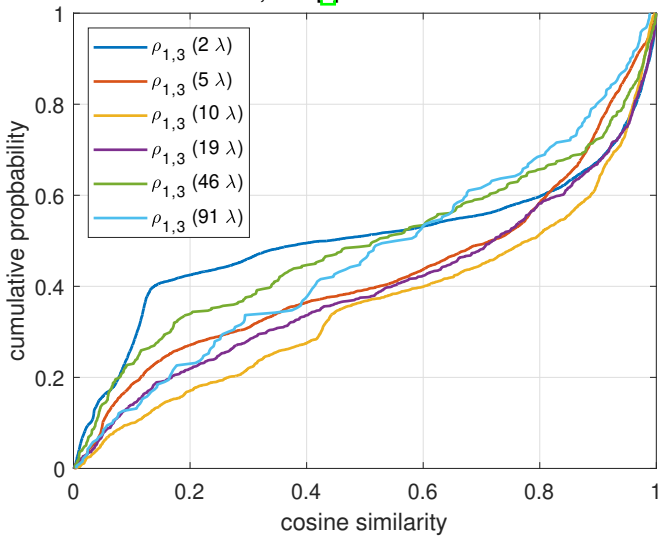

FIGURE 23. Empirically calculated CDF for the cosime simularity between 3.2 GHz and 62.35 GHz for the LOS region between t_1 and t_2, from [4].

VII. Conclusion

This paper has provided an overview of the coordinated experimental activities of four research organizations, TUW, AIT, BUT, and USC for the measurement of mmWave V2V and V2I channels. We presented a summary of channel sounder design, measurement campaign design, and measurement results. From these, we can draw a number of conclusions:

- *Channel sounder design:*
  - The channel sounder design is critically impacted by the goals of the measurement campaigns. Bandwidth, length of sounding sequence, repetition frequency of the sounding signal, and duration of the acquired data set need to be traded off, given the constraints on available equipment and the particular measurement scenario (including vehicular speed). There is no single ”best” configuration.
  - The choice of the employed antennas will be different for V2I measurements where only a small stretch of road is of interest, to V2I measurements where a longer stretch of road is of interest and thus a manual tracking of the car by the horn antenna might be preferable, to V2V passing measurements, where omnidirectional antennas are essential. Use of directionally resolved sounders, either based on the ReRoMA principle as in this work, or on phased arrays, largely solves this dilemma but might face other obstacles, including whether sufficiently fast sampling is available.
- *Measurement campaign planning:*
  - The measurement results depend both on what event is to be measured (convoy, overtaking, V2I, etc.), and the details of the surrounding environment. For the former aspect, the choice of the antennas also plays a critical role, as discussed above.
  - Even environmental scenarios that are nominally the same, such as ”urban street canyon” can show significant differences in the details of the environment, which also lead to significant differences in the CIRs and the channel statistics. Street canyons abutted by large buildings (and little vegetation between traffic lanes and buildings) create much more pronounced reflections than wide streets with trees and greenery on the sides, even when buildings are present.
- *Important propagation effects:*
  - Multiple of our measurement campaigns have shown that small objects close to the street, such as lamp posts, garbage containers, and parked cars, can give rise to strong echoes, in many cases with amplitudes that are comparable to the reflections from buildings.
  - Vehicles overtaking the two cars communicating with each other do not significantly impact the total received power and RMS delay spread, but do impact the Doppler spread, with trucks giving rise to multiple components due to reflections from different parts of the truck.
  - While the LOS component is always dominant (when not blocked), other reflected MPCs can carry significant power, often within 10 dB of the LOS power. This increases the chance that communication is feasible even in blocked LOS situations.
- *Channel statistics:*
  - RMS delay spreads vary significantly between the different measured scenarios. The most important factor is the choice of the antennas - omnidirectional delay spreads tend to be larger than max-dir delay spreads by a factor on the order of 5. Still, in all analyzed cases, the RMS delay spread was below 100 ns.
  - The channel properties are clearly nonstationary, with the stationarity times depending on the definition (synchronization to the LOS component or not).
  - The V2I channel offers beam diversity, with different components visible in the DSD depending on the beam orientation on the car-mounted link end.
  - The channel characteristics in the 3, 30, and 60 GHz band show significant correlation, with median cosine similarities around 0.5.
- *System implications:*
  - A cyclic prefix (CP) on the order of tens, or a few hundred, nanoseconds, is sufficient for most measured situations, in particular when a low-order modulation format is used and thus the fraction of the energy of the impulse response arriving outside the CP need not be extremely small. The shortest CP defined in 5G, namely 290 ns, is sufficient for all measured situations.
  - Algorithms for rapid adaptation of the transmission/reception direction are important, in particular for V2V situations when one car turns around the corner, but also V2I, e.g., when a vehicle passes under an infrastructure node.
  - The large Doppler spreads require a very fast adaption of all receiver components that need to adjust to the small-scale fading state. Directional antennas at both link ends can mitigate, but not eliminate this challenge.
  - The short stationarity times imply that the common assumption of second-order channel statistics being static over the time period of interest (data transmission) may not hold in V2X communications.

While the results from these campaigns provide important insights into the propagation mechanism and channel statistics for mmWave V2X channels, they are far from the ”last word” on this topic, and much more work should be conducted in particular in light of the future standardization of mmWave V2X communications in advanced 5G and 6G standards.

Acknowledgments

We would like to thank the METRANS project, and in particular Genevieve Giuliano, Cort Brinkerhoff and Katrina Soriano for their kind help in handling many administrative issues over the duration of the project. We would like to also thank former WiDeS@USC group members, especially Dr. Seun Sangodoyin, Dr. Guillermo Castro, and Dr. Jorge Gomez-Ponce, for their help in the hardware design and measurement campaign. Furthermore we would like to thank David Löschenbrand, Stefan Zelenbaba, Anja Dakić, Laura Bernadó and Benjmin Rainer for supporting the measurement campaigns at AIT. We would also like to extend our thanks to Herbert Groll for his support in evaluating the TUW measurement results.

Conflict of interest statement Three of the authors (AFM, CFM, and HH) are co-inventors on a patent for a measurement apparatus results from which are described in the paper [61].

REFERENCES

[1] C. F. Mecklenbrauker, A. F. Molisch, J. Karedal, F. Tufvesson, A. Paier, L. Bernadó, T. Zemen, O. Klemp, and N. Czink, “Vehicular channel characterization and its implications for wireless system design and performance,” *Proceedings of the IEEE*, vol. 99, no. 7, pp. 1189–1212, 2011.

[2] M. Hofer, D. Löschenbrand, J. Blumenstein, H. Groll, S. Zelenbaba, B. Rainer, L. Bernado, J. Vychodil, T. Mikulasek, E. Zöchmann, S. Sangodoyin, H. Hammoud, B. Schrenk, R. Langwieser, S. Pratschner, A. Prokes, A. F. Molisch, C. F. Mecklenbräuker, and T. Zemen, “Wireless Vehicular Multiband Measurements in Centimeterwave and Millimeterwave Bands,” in *IEEE 32nd Annual International Symposium on Personal, Indoor and Mobile Radio Communications (PIMRC)*, 2021.

[3] M. Hofer, D. Löschenbrand, S. Zelenbaba, A. Dakić, B. Rainer, and T. Zemen, “Wireless 3 GHz and 30 GHz Vehicle-to-Vehicle Measurements in an Urban Street Scenario,” in *IEEE 96th Vehicular Technology Conference (VTC-Fall)*, 2022, pp. 836–841.

[4] M. Hofer, D. Löschenbrand, F. Pasic, B. Rainer, J. Blumenstein, C. F. Mecklenbräuker, S. Sangodoyin, H. Hammoud, G. Matz, A. F. Molisch, , and T. Zemen, “Similarity of wireless multiband propagation in urban vehicular-to-infrastructure scenarios,” in *IEEE Annual International Symposium on Personal, Indoor and Mobile Radio Communications (PIMRC)*. Valencia, Spain: IEEE, September 2024.

[5] H. Hammoud, Y. Zhang, Z. Cheng, S. Sangodoyin, M. Hofer, F. Pasic, T. M. Pohl, R. Závorka, A. Prokes, T. Zemen *et al.*, “A novel low-cost channel sounder for double-directionally resolved measurements in the mmWave band,” in *IEEE International Conference on Communications (ICC)*. Denver, CO, USA: IEEE, June 2024, pp. 3195–3201.

[6] H. Hammoud, Y. Zhang, Z. Cheng, S. Sangodoyin, M. Hofer, F. Pasic, T. M. Pohl, R. Závorka, A. Prokes, T. Zemen, C. Mecklenbräuker, and A. F. Molisch, “A novel low-cost channel sounder for double-directionally resolved measurements in the mmwave band,” *IEEE Transactions on Wireless Communications*, vol. early access, 2024.

[7] H. Hammoud, Y. Zhang, Z. Cheng, S. Sangodoyin, M. Hofer, F. Pasic, T. Pohl, R. Závorka, A. Prokeš, T. Zemen, C. F. Mecklenbräuker, and A. F. Molisch, “Double-directional v2v channel measurement using reroma at 60 ghz,” *arxiv:2412.01165*, 2024.

[8] H. Groll *et al.*, “Sparsity in the delay-Doppler domain for measured 60 GHz vehicle-to-infrastructure communication channels,” in *2019 IEEE International Conference on Communications Workshops (ICC Workshops)*. Shanghai, China: IEEE, May 2019.

[9] E. Zöchmann *et al.*, “Position-specific statistics of 60 GHz vehicular channels during overtaking,” *IEEE Access*, vol. 7, pp. 14 216–14 232, 2019.

[10] E. Zochmann, C. F. Mecklenbräuker, M. Lerch, S. Pratschner, M. Hofer, D. Löschenbrand, J. Blumenstein, S. Sangodoyin, G. Artner, S. Caban, T. Zemen, A. Prokeš, M. Rupp, and A. F. Molisch, “Measured delay and Doppler profiles of overtaking vehicles at 60 GHz,” in *12th European Conference on Antennas and Propagation (EuCAP)*, London, UK, December 2018.

[11] E. Zöchmann, M. Hofer, M. Lerch, J. Blumenstein, S. Sangodoyin, H. Groll, S. Pratschner, S. Caban, D. Löschenbrand, L. BernadÓ, T. Zemen, A. Prokes, M. Rupp, C. F. Mecklenbräuker, and A. F. Molisch, “Statistical evaluation of delay and Doppler spread in 60 GHz vehicle-to-vehicle channels during overtaking,” in *IEEE-APS Topical Conference on Antennas and Propagation in Wireless Communications (APWC)*. Cartagena, Colombia: IEEE, September 2018.

[12] A. Prokes, J. Blumenstein, J. Vychodil, T. Mikulasek, R. Marsalek, E. Zöchmann, H. Groll, C. F. Mecklenbräuker, T. Zemen, A. Chandra *et al.*, “Multipath propagation analysis for vehicle-to-infrastructure communication at 60 GHz,” in *2019 IEEE Vehicular Networking Conference (VNC)*. IEEE, 2019, pp. 1–8.

[13] A. Prokes, J. Vychodil, T. Mikulasek, J. Blumenstein, E. Zöchmann, H. Groll, C. F. Mecklenbräuker, M. Hofer, D. Löschenbrand, L. Bernadó *et al.*, “Time-domain broadband 60 GHz channel sounder for vehicle-to-vehicle channel measurement,” in *IEEE Vehicular Networking Conference (VNC)*. Taipei, Taiwan: IEEE, December 2018.

[14] J. Vychodil, M. Pospisil, A. Prokes, and J. Blumenstein, “Millimetre wave band time domain channel sounder,” *IET Communications*, vol. 13, no. 3, pp. 331–338, 2019.

[15] A. F. Molisch, F. Tufvesson, J. Karedal, and C. F. Mecklenbrauker, “A survey on vehicle-to-vehicle propagation channels,” *IEEE Wireless Communications*, vol. 16, no. 6, pp. 12–22, 2009.

[16] C.-X. Wang, X. Cheng, and D. I. Laurenson, “Vehicle-to-vehicle channel modeling and measurements: recent advances and future challenges,” *IEEE communications magazine*, vol. 47, no. 11, pp. 96–103, 2009.

[17] D. W. Matolak, “Modeling the vehicle-to-vehicle propagation channel: A review,” *Radio Science*, vol. 49, no. 9, pp. 721–736, 2014.

[18] W. Viriyasitavat, M. Boban, H.-M. Tsai, and A. Vasilakos, “Vehicular communications: Survey and challenges of channel and propagation models,” *IEEE Vehicular Technology Magazine*, vol. 10, no. 2, pp. 55–66, 2015.

[19] F. A. Rodríguez-Corbo, L. Azpilicueta, M. Celaya-Echarri, A. V. Alejos, and F. Falcone, “Propagation models in vehicular communications,” *IEEE Access*, vol. 9, pp. 15 902–15 913, 2021.

[20] F. Jameel, S. Wyne, S. J. Nawaz, and Z. Chang, “Propagation channels for mmwave vehicular communications: State-of-the-art and future research directions,” *IEEE Wireless Communications*, vol. 26, no. 1, pp. 144–150, 2018.

[21] R. He, C. Schneider, B. Ai, G. Wang, Z. Zhong, D. A. Dupleich, R. S. Thomae, M. Boban, J. Luo, and Y. Zhang, “Propagation channels of 5G millimeter-wave vehicle-to-vehicle communications: Recent advances and future challenges,” *IEEE vehicular technology magazine*, vol. 15, no. 1, pp. 16–26, 2019.

[22] A. F. Molisch, *Wireless Communications: From Fundamentals to Beyond 5G*, 3rd ed. IEEE Press - Wiley, 2023.

[23] W. Schafer, “Channel modelling of short-range radio links at 60 GHz for mobile intervehicle communication,” in *41st IEEE Vehicular Technology Conference (VTC)*. St. Louis, MO, USA: IEEE, May 1991, pp. 314–319.

[24] ——, “A new deterministic/stochastic approach to model the inter-vehicle channel at 60 GHz,” in *IEEE 43rd Vehicular Technology Conference (VTC)*. Secaucus, NJ, USA: IEEE, May 1993, pp. 112–115.

[25] K. Mizutani and R. Kohno, “Analysis of multipath fading due to two-ray fading and vertical fluctuation of the vehicles in ITS inter-vehicle communications,” in *IEEE 5th International Conference on Intelligent Transportation Systems*. Singapore: IEEE, September 2002, pp. 318–323.

[26] K. Sato and M. Fujise, "Propagation measurements for inter-vehicle communication in 76-GHz band," in *6th International Conference on ITS Telecommunications*. Chengdu, China: IEEE, June 2006, pp. 408–411.

[27] M. Heddebaut, F. Elbahhar, C. Loyez, N. Obeid, N. Rolland, A. Rivenq, and J.-M. Rouvaen, "Millimeter-wave communicating-radars for enhanced vehicle-to-vehicle communications," *Transportation Research Part C: Emerging Technologies*, vol. 18, no. 3, pp. 440–456, 2010.

[28] R. Schneider, D. Didascalou, and W. Wiesbeck, "Impact of road surfaces on millimeter-wave propagation," *IEEE Transactions on Vehicular Technology*, vol. 49, no. 4, pp. 1314–1320, 2000.

[29] M. G. Sánchez, M. P. Táboas, and E. L. Cid, "Millimeter wave radio channel characterization for 5G vehicle-to-vehicle communications," *Measurement*, vol. 95, pp. 223–229, 2017.

[30] S. Takahashi, A. Kato, K. Sato, and M. Fujise, "Distance dependence of path loss for millimeter wave inter-vehicle communications," in *IEEE 58th Vehicular Technology Conference (VTC-Fall)*, vol. 1. Orlando, FL, USA: IEEE, October 2003, pp. 26–30.

[31] H. Wang, X. Yin, J. Rodríguez-Piñeiro, J. Lee, and M.-D. Kim, "Shadowing and multipath-fading statistics at 2.4 GHz and 39 GHz in vehicle-to-vehicle scenarios," in *14th European Conference on Antennas and Propagation (EuCAP)*. Copenhagen, Denmark: IEEE, March 2020.

[32] A. Ghosh, A. Chandra, T. Mikulasek, A. Prokes, J. Wojtun, J. M. Kelner, and C. Ziolkowski, "Vehicle-to-vehicle path loss modeling at millimeter-wave band for crossing cars," *IEEE Antennas and Wireless Propagation Letters*, vol. 22, no. 9, pp. 2125–2129, 2023.

[33] J. Hoellinger, G. Makhoul, R. D'Errico, and T. Marsault, "V2v dynamic channel characterization in 5G mmWave band," in *International Symposium on Antennas and Propagation (ISAP)*. Sydney, Australia: IEEE, November 2022, pp. 525–526.

[34] D. Dupleich, R. Müller, S. Skoblikov, C. Schneider, J. Luo, M. Boban, G. Del Galdo, and R. Thomä, "Multi-band characterization of path-loss, delay, and angular spread in V2V links," in *IEEE 29th Annual International Symposium on Personal, Indoor and Mobile Radio Communications (PIMRC)*. Bologna, Italy: IEEE, September 2018, pp. 85–90.

[35] D. Dupleich, R. Muller, C. Schneider, S. Skoblikov, J. Luo, M. Boban, G. Del Galdo, and R. Thoma, "Multi-band vehicle to vehicle channel measurements from 6 GHz to 60 GHz at T-intersection," in *IEEE 2nd Connected and Automated Vehicles Symposium (CAVS)*. Honolulu, HI, USA: IEEE, September 2019.

[36] J. M. Eckhardt, V. Petrov, D. Moltchanov, Y. Koucheryavy, and T. Kürner, "Channel measurements and modeling for low-terahertz band vehicular communications," *IEEE Journal on Selected Areas in Communications*, vol. 39, no. 6, pp. 1590–1603, 2021.

[37] J. Huang, C.-X. Wang, H. Chang, J. Sun, and X. Gao, "Multi-frequency multi-scenario millimeter wave MIMO channel measurements and modeling for B5G wireless communication systems," *IEEE Journal on Selected Areas in Communications*, vol. 38, no. 9, pp. 2010–2025, 2020.

[38] M. Soliman, P. Unterhuber, F. De Ponte Muller, M. Schmidhammer, S. Sand, and A. Dekorsy, "Design and evaluation of a millimeter wave channel sounder for dynamic propagation measurements," in *IEEE 88th Vehicular Technology Conference (VTC-Fall)*, Chicago, IL, USA, August 2018.

[39] Z. Zhang, R. He, B. Ai, M. Yang, X. Zhang, Z. Qi, and Y. Yuan, "Channel measurements and modeling for dynamic vehicular ISAC scenarios at 28 GHz," *arXiv preprint arXiv:2403.00605*, 2024.

[40] N. Attwood, F. Gallee, P. Pajusco, and M. Berbineau, "mmWave channel sounding for vehicular communications," in *18th European Conference on Antennas and Propagation (EuCAP)*, Glasgow, United Kingdom, March 2024.

[41] A. Chopra *et al.*, "Real-time millimeter wave omnidirectional channel sounder using phased array antennas," in *IEEE Global Communications Conference (GLOBECOM)*. Taipei, Taiwan: IEEE, December 2020.

[42] ——, "A real-time millimeter wave V2V channel sounder," in *IEEE Wireless Communications and Networking Conference (WCNC)*. Austin, TX, USA: IEEE, April 2022, pp. 2607–2612.

[43] O. Kanhere *et al.*, "Performance impact analysis of beam switching in millimeter wave vehicular communications," in *IEEE 93rd Vehicular Technology Conference (VTC-Spring)*. Helsinki, Finland: IEEE, April 2021.

[44] C. U. Bas, R. Wang, S. Sangodoyin, D. Psychoudakis, T. Henige, R. Monroe, J. Park, C. J. Zhang, and A. F. Molisch, "Real-time millimeter-wave mimo channel sounder for dynamic directional measurements," *IEEE Transactions on Vehicular Technology*, vol. 68, no. 9, pp. 8775–8789, 2019.

[45] A. Yamamoto, K. Ogawa, T. Horimatsu, A. Kato, and M. Fujise, "Path-loss prediction models for intervehicle communication at 60 GHz," *IEEE Transactions on Vehicular Technology*, vol. 57, no. 1, pp. 65–78, 2008.

[46] P. Kryszkiewicz, A. Kliks, P. Sroka, and M. Sybis, "The impact of blocking cars on pathloss within a platoon: Measurements for 26 GHz band," in *International Conference on Software, Telecommunications and Computer Networks (SoftCOM)*. Split, Hvar, Croatia: IEEE, September 2021.

[47] M. Boban, D. Dupleich, N. Iqbal, J. Luo, C. Schneider, R. Müller, Z. Yu, D. Steer, T. Jämsä, J. Li *et al.*, "Multi-band vehicle-to-vehicle channel characterization in the presence of vehicle blockage," *IEEE Access*, vol. 7, pp. 9724–9735, 2019.

[48] J.-J. Park, J. Lee, J. Liang, K.-W. Kim, K.-C. Lee, and M.-D. Kim, "Millimeter wave vehicular blockage characteristics based on 28 GHz measurements," in *IEEE 86th Vehicular Technology Conference (VTC-Fall)*. Toronto, ON, Canada: IEEE, September 2017.

[49] M. Rodriguez, M. Diago-Mosquera, R. Feick, M. Almendra-Villalobos, D. Chizhik, J. Sapis, J. Du, and R. Valenzuela, "Fading statics of 28 GHz LOS link blockage due to vehicular traffic," *IEEE Transactions on Vehicular Technology*, 2024.

[50] C. U. Bas, R. Wang, S. Sangodoyin, S. Hur, K. Whang, J. Park, J. Zhang, and A. F. Molisch, "Dynamic double directional propagation channel measurements at 28 ghz-invited paper," in *2018 IEEE 87th Vehicular Technology Conference (VTC Spring)*. IEEE, 2018, pp. 1–6.

[51] D. Yan, K. Guan, D. He, J. Kim, H. Chung, D. Tian, and Z. Zhong, "Blockage effects of road bridge on mmWave channels for intelligent autonomous vehicles," *IEEE Transactions on Intelligent Transportation Systems*, vol. 25, no. 3, pp. 2908–2919, 2023.

[52] K. Sato, M. Fujise, R. Tachita, E. Hase, and T. Nose, "Propagation in ROF road-vehicle communication system using millimeter wave," in *Proceedings of the IEEE International Vehicle Electronics Conference (IVEC)*. Tottori, Japan: IEEE, September 2001, pp. 131–135.

[53] I. A. Hemadeh, K. Satyanarayana, M. El-Hajjar, and L. Hanzo, "Millimeter-wave communications: Physical channel models, design considerations, antenna constructions, and link-budget," *IEEE Communications Surveys & Tutorials*, vol. 20, no. 2, pp. 870–913, 2017.

[54] J. Huang *et al.*, "5G millimeter wave channel sounders, measurements, and models: Recent developments and future challenges," *IEEE Communications Magazine*, vol. 57, no. 1, pp. 138–145, 2018.

[55] A. F. Molisch, T. Choi, N. Abbasi, F. Rottenberg, and J. Zhang, "Millimeter-wave channels," *Wiley 5G Ref: The Essential 5G Reference Online*, pp. 1–46, 2019.

[56] T. S. Rappaport, K. A. Remley, C. Gentile, A. F. Molisch, and A. Zajić, *Radio Propagation Measurements and Channel Modeling: Best Practices for Millimeter-Wave and Sub-Terahertz Frequencies*. Cambridge University Press, 2022.

[57] S. Sangodoyin, J. Salmi, S. Niranjayan, and A. F. Molisch, "Real-time ultrawideband MIMO channel sounding," in *6th European Conference on Antennas and Propagation (EUCAP)*, Prague, Czech Republic, March 2012, pp. 2303–2307.

[58] T. Mikulasek, J. Blumenstein, and A. Prokes, "Antennas utilized for intra-vehicle 3–11 GHz and 55–65 GHz channel measurement," in *Progress in Electromagnetic Research Symposium (PIERS)*, Shanghai, China, August 2016, pp. 4258–4262.

[59] *Device Specifications, NI USRP-2594R, 10 MHz to 6 GHz Tunable RF Transceiver*, National Instruments.

[60] D. Löschenbrand, M. Hofer, L. Bernadó, G. Humer, B. Schrenk, S. Zelenbaba, and T. Zemen, "Distributed massive MIMO channel measurements in urban vehicular scenario," in *13th European Conference on Antennas and Propagation (EuCAP)*, Krakow, Poland, April 2019.

[61] A. F. Molisch *et al.*, "Spinning directional antenna in centimeter and millimeter wave bands," Patent WO 2022155493 A1, sep 2022, available at: https://patents.google.com/patent/WO2022155493A1/en.

[62] J. Gomez-Ponce, N. A. Abbasi, Z. Cheng, S. Abu-Surra, G. Xu, J. Zhang, and A. F. Molisch, "Impact of noisy measurements with Fourier-based evaluation on condensed channel parameters," *IEEE Transactions on Wireless Communications*, vol. 23, no. 8, pp. 8136 – 8152, August 2024.
[63] D. B. Percival and A. T. Walden, *Spectral Analysis for Physical Applications*. Cambridge University Press, 1963.
[64] A. Molisch, "Statistical properties of the RMS delay-spread of mobile radio channels with independent rayleigh-fading paths," *IEEE Transactions on Vehicular Technology*, vol. 45, no. 1, pp. 201–204, 1996.
[65] L. Bernadó, T. Zemen, F. Tufvesson, A. F. Molisch, and C. F. Mecklenbrauker, "Delay and Doppler spreads of nonstationary vehicular channels for safety-relevant scenarios," *IEEE Trans. Veh. Technol.*, vol. 63, no. 1, pp. 82–93, Jan. 2014.

Andy Molisch received his degrees (Dipl.Ing. 1990, PhD 1994, Habilitation 1999) from the Technical University Vienna, Austria. He spent the next 10 years in industry, at FTW, AT&T (Bell) Laboratories, and Mitsubishi Electric Research Labs (where he rose to Chief Wireless Standards Architect). In 2009 he joined the University of Southern California (USC) in Los Angeles, CA, as Professor, and founded the Wireless Devices and Systems (WiDeS) group. In 2017, he was appointed to the Solomon Golomb - Andrew and Erna Viterbi Chair.

His research interests revolve around wireless propagation channels, wireless systems design, and their interaction. Recently, his main interests have been wireless channel measurement and modeling for 5G and 6G systems, joint communication-caching-computation, hybrid beamforming, UWB/TOA based localization, and novel modulation/multiple access methods. Overall, he has published 5 books (among them the textbook "Wireless Communications", third edition in 2023), 22 book chapters, $>$ 300 journal papers, and $>$ 400 conference papers. He is also the inventor of 80 patents, and co-author of some 70 standards contributions. His work has been cited more than 74,000 times, his h-index is 114, and he is a Clarivate Highly Cited Researcher.

Dr. Molisch has been an Editor of a number of journals and special issues, General Chair, Technical Program Committee Chair, or Symposium Chair of multiple international conferences, as well as Chairperson of various international standardization groups. He is a Fellow of the National Academy of Inventors, Fellow of the AAAS, Fellow of the IEEE, Fellow of the IET, an IEEE Distinguished Lecturer, and a member of the Austrian Academy of Sciences. He has received numerous awards, among them the IET Achievement Medal, the Technical Achievement Awards of IEEE Vehicular Technology Society (Evans Avant-Garde Award) and the IEEE Communications Society (Edwin Howard Armstrong Award), and the Technical Field Award of the IEEE for Communications (Eric Sumner Award).

Christoph F. Mecklenbräuker (Senior Member, IEEE) received the Dipl.-Ing. degree (Hons.) in electrical engineering from Technische Universität Wien, Vienna, Austria, in 1992, and the Dr.-Ing. degree (Hons.) from Ruhr- Universität Bochum, Bochum, Germany, in 1998. From 1997 to 2000, he was with Siemens AG, Austria, and engaged in the standardization of UMTS. From 2000 to 2006, he was a Senior Researcher with the Telecommunications Research Center Vienna (FTW), Vienna. In 2006, he joined TU Wien as a Full Professor. From 2009 to 2016, he led the Christian Doppler Laboratory for Wireless Technologies for Sustainable Mobility. He has authored approximately 250 papers in international journals and conferences, for which he has also served as a reviewer and was granted several patents in the field of mobile cellular networks. His current research interests include 5G/6G radio interfaces (vehicular connectivity, localization, and sensor networks) and millimeter waves. He is a member of the Antennas and Propagation Society, the Intelligent Transportation Society, the Vehicular Technology Society, the Signal Processing Society, VDE, and EURASIP. His doctoral dissertation received the Gert-Massenberg Prize, in 1998. He is the Councilor of the IEEE Student Branch Wien.

Thomas Zemen (S'03 -M'05 -SM'10) Thomas Zemen received the Dipl.-Ing. degree, the doctoral degree and the Venia Docendi (Habilitation) from Technische Universität Wien (TU Wien).

He joined AIT Austrian Institute of Technology in 2014 and is Principal Scientist since 2021 leading the wireless research group. Previously, Thomas Zemen worked for Siemens AG Austria and the Telecommunication Research Center Vienna (FTW).

Mr. Zemen has published four book chapters, 49 journal papers, more than 160 conference communications, and two patents. His research interests are sustainable 6G physical layer radio communication technologies for time-sensitive applications with a focus on distributed MIMO systems, reconfigurable intelligent surfaces, multi-band communications, joint communication and sensing, and site-specific radio channel models. Dr. Zemen is docent at the Vienna University of Technology, teaching advanced wireless communications.

Ales Prokes received the M.Sc., Ph.D., and the Habilitation degrees from Brno University of Technology (BUT), in 1988, 1999, and 2006, respectively. Since 1990, he has been with the Faculty of Electrical Engineering and Communication, BUT, where he is currently a Professor. Since 2013, he has been the Head of the Research Center of Sensor, Information and Communication Systems, Radio-Frequency Systems Group. His research interests include measurement and modeling of channels for V2X communication, optimization and design of optical receivers and transmitters for free-space optics (FSO) systems, the influence of atmospheric effects on optical signal propagation, and software-defined radio.

Markus Hofer received the Dipl.-Ing. degree in 2013 and the doctoral degree in 2019, both from the Technical University of Vienna. From 2013 to 2015 he was with the FTW Telecommunications Research Center Vienna working as a researcher in the Signal and Information Processing department. He has been with the AIT Austrian Institute of Technology, Vienna since 2015 and is working as a Scientist in the Research group for ultrareliable wireless communications. His research interests include ultra-reliable low latency wireless communications, mmWave and multi-band communications, reflective intelligent surfaces, cell-free massive MIMO, time-variant channel measurements, modeling and realtime emulation; time-variant channel estimation, 5G massive MIMO systems and software-defined radio rapid prototyping.

Faruk Pasic (Graduate Student Member, IEEE) received the B.Sc. degree in electrical engineering and the Dipl. Ing. degree (M.Sc. equivalent) in telecommunications from the University of Sarajevo, Bosnia and Herzegovina and TU Wien, Austria, in 2017 and 2021, respectively. In 2024, he was a Visiting Researcher at the University of Southern California, CA, USA. He is currently pursuing his Ph.D. degree in telecommunications engineering at the Institute of Telecommunications, TU Wien. His research interests include wireless channel measurements and modeling, channel estimation, mmWave technology, MIMO systems, and out-of-band aided communication.

Hussein Hammoud received his M.S. degree in Communication and Radio Engineering from the University of Southern California (USC). In 2024, he finished his Ph.D. at USC, where his research focused on millimeter-wave communications and advanced channel modeling techniques. His work primarily involves the design and implementation of channel sounding systems, as well as the analysis of propagation characteristics. He also holds a patent.